Department of Precision and Microsystems Engineering

Lightsail design with neural optimization of topology

Lucas Norder

Report no : 2022.003
Coach : Dr. R.A.Norte, Dr. M.A. Bessa
Specialisation : MSD & MEA
Type of report : MSc Thesis
Date : 2 February 2022

LIGHTSAIL DESIGN WITH NEURAL OPTIMIZATION OF TOPOLOGY

MSc Thesis

by

Lucas NORDER

Student Number:	4355563	
Thesis advisor:	Dr. M.A. Bessa,	TU Delft, 3mE faculty
	Dr. R.A. Norte,	TU Delft, 3mE faculty

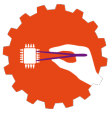

Precision and
Microsystems
Engineering

Materials Science
and Engineering

SUMMARY

Breakthrough initiatives have started the Starshot initiative to stimulate the design of a lightsail to reach Alpha Centauri within 20 years. This technology is based on generating an optical force on a reflective lightweight thin-film material by projecting a high power Earth-based laser on it. A photonic crystal design is necessary to obtain high reflectivity and comply with the mass constrain. In literature, thin-film designs have been shown to achieve high reflectivity. However, non of the designs are suitable for a lightsail because they do not sufficiently consider operational conditions (e.g. manufacturability, flight stability and maximum heating). For a practical design, multiple objectives must be combined to comply with all the operational requirements.

Literature has shown that traditional TO can be a valuable tool for designing nanophotonic devices. TO allows optimizing a large design space, which can result in highly optimized and non-trivial structures. However, there are still a few significant drawbacks that can be improved. A significant disadvantage of the TO methods is that the optimizer can get stuck in local optima because TO methods are not global optimizers. Many optimizations with different initialization need to be considered to mitigate this, making it a time-consuming process. Another disadvantage of TO algorithms is that they are computationally heavy and susceptible to optimization parameters, making it time-consuming to derive optimized structures. ML-based TO has proven to solve some of these problems and generate better and more general designs in less time. However, implementing these ML-based TO is a non-trivial process.

In this work, a convolutional neural network (CNN) based TO methodology is extended to optimize a 2D photonic crystal used to design a lightsail. The CNN-TO performance is compared to a more conventional method of moving asymptotes (MMA) based TO by optimizing a photonic crystal unit-cell for the 2016 Starshot Initiative parameters. The CNN-TO requires 10%-40% fewer iterations than MMA-TO to reach better performance under different operational conditions. The generated design turned out to be easy to fabricate, allowing them to be produced with optical lithography. Additionally, a study regarding the design challenges of the lightsail has been performed, showing the sensitivity of the resulting design to varying objectives and materials. Therefore, underlining the necessity of considering multiple operating conditions (e.g. laser alignment and cooling) within the design process.

Contents

List of Figures

LIST OF TABLES

1

INTRODUCTION

At the moment, the man-made object furthest from the earth is the Voyager 1 (NASA, n.d.). Although this spacecraft has seen our solar system and beyond, it only travelled 0.5% of the distance to the nearest solar system after 47 years of service. New spacecraft are required to explore these unknown worlds. Breakthrough Initiatives started the Starshot Initiative in 2016 to stimulate the development of lightsails (Breakthrough Initiatives, n.d.). This spacecraft aims to reach Alpha Centauri (i.e. the nearest star to earth) within 20 years by reaching speeds up to 20% of the speed of light. This technology is based on generating an optical force on a reflective lightweight thin-film material by projecting a high power earth-based laser on it.

Traditional metallic reflectors cannot be used because of their high optical absorption. Semiconductors can meet the operating requirements as they have a high refractive index and low optical absorption. To meet the mass and reflectivity requirements using semiconductors, an approximately 100 atomic layers thick sail with a photonic design is necessary (Atwater et al., 2018).

The most promising design is the 2D photonic crystal (PhC), as it had been shown to provide high reflectivity at the critical area density (Norte et al., 2016). Although 2D PhC's have proven to be effective reflectors even with simple designs, most designs are not optimized for a lightsail. The current designs are not suitable for a lightsail because they do not sufficiently consider operational conditions (e.g. manufacturability, flight stability and maximum heating). For a practical designs multiple objectives need to be combined to comply with all the operational requirements.

Traditionally, optimizing photonic structures is a highly iterative process executed by experienced people (Liu et al., 2018). The optimization process is involved as nanophotonic devices are high dimensional, non-unique and can only be analyzed using computationally heavy algorithms. Recently, inverse design methods like topology optimization (TO) have become more prevalent in many fields. Not only traditional TO but also new machine learning-based TO have been proven successful (Hoyer et al., 2019). The machine learning-based TO can optimize faster, generate more general designs and optimize closer to a global optimum. Furthermore, these different inverse design methods

have proven to be effective tools for the design of the nanophotonic structure (Molesky et al., 2018) because they can consider many design variables and can result in non-trivial designs.

In this work the novel machine learning (ML) based TO proposed in Hoyer et al., 2019 is applied to lightsail design by changing the physics analysis and modifying the neural network. This free-form TO does not require any training data and has proven successful for structural engineering. The work of Jin et al., 2020 acts as a baseline for this investigation, as they implemented a conventional TO approach to design a 2D PhC unit-cell for a lightsail following the Starshot parameters. The physics analysis from this method is implemented in the machine learning TO and the results are compared.

This work starts with a literature review discussing the design challenges of a lightsail and reviewing existing solutions from which design considerations, material choice, production techniques, and concept designs are explored. In addition, this literature review also elaborates on the computational design techniques for designing a lightsail. Instead of solely focusing on traditional topology optimization strategies, novel machine learning-based topology optimization algorithms are also presented. Chapter 3 will discuss the new work performed in the thesis. First, a novel ML-based TO method is benchmarked against a traditional TO. Moreover, new designs are generated with the ML-based TO by considering additional operational conditions and different materials. This chapter is followed by discussing the obtained results and recommendations for future work. The last part of the thesis is the supporting information of the work presented in chapter 3.

2

LITERATURE REVIEW

ABSTRACT

This literature review elaborates on the design of a lightsail. The idea for this review originated from the Starshot initiative, which was started by Breakthrough Initiatives to intensify the research on lightsail propelled satellites that can reach Alpha Centauri within 20 years. This work starts discussing the design challenges regarding a lightsail and reviewing existing solutions from which design considerations, material choice, production techniques, and concept designs are explored. In addition, this literature review also elaborates on the computational design techniques for designing a lightsail. Instead of solely focusing on traditional topology optimization strategies, novel machine learning-based topology optimization algorithms are also presented. This work identified the following knowledge gaps. In literature, thin-film designs have been shown to achieve high reflectivity. However, non of the designs are suitable for a lightsail because they do not consider operational conditions (e.g. manufacturability, flight stability and maximum heating). So far, only single objective studies have been performed, but for a practical design, multiple objectives need to be combined to comply with all the operational requirements. A photonic crystal design of the sail is necessary to obtain high reflectivity and comply with the mass constrain. Inverse design has proven to be an effective design methodology for nanophotonic structures. Notably, a novel free-form machine learning-based topology optimization technique that does not require any training data has proven successful for structural engineering. However, no equivalent topology optimization method has been implemented in photonics yet. For the thesis, the machinelearning based topology optimization approach as proposed by Hoyer et al., 2019 is applied to the lightsail design. It is expected that this method can result in a fast optimization algorithm and in designs close to the global optimum compared to a traditional topology optimization.

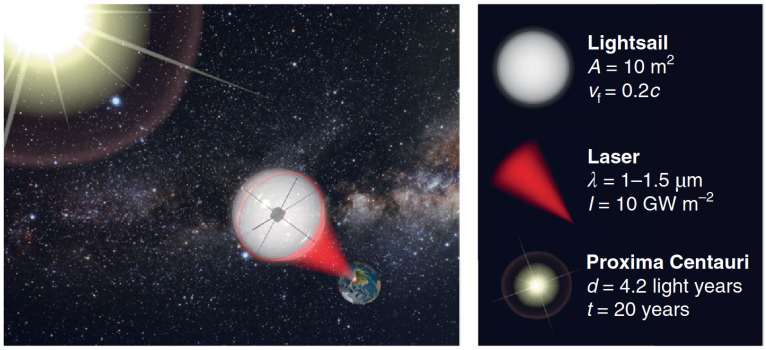

Figure 2.1: Illustration of the lightsail as envisioned in the Starshot initiative, with the standard Starshot parameters (Atwater et al., 2018).

2.1. STARSHOT INITIATIVE

Human fascination with space exploration has been expressed in different ways. Designing machines to explore the planets in our solar system, and even beyond our solar system is critically important to this endeavor. However, the design challenges involved are so stringent that innovative solutions are required. One of these innovative ideas is the use of a lightsail for deep space travel, which is based on propelling an ultra-light satellite by focusing a high power earth-based laser on a thin sail-like material attached to the satellite. This laser could push the satellite to 20% of the speed of light. Decades ago, this idea seemed far-fetched, but recent technological advances in multiple fields (e.g. materials science, nano production and laser technology) opened the possibility for this idea. Breakthrough initiatives started the Starshot initiative to stimulate the research for the topics that remain unsolved (Breakthrough Initiatives, n.d.). This initiative aims to design a lightsail propelled satellite that can reach Alpha Centauri within 20 years and send pictures of Alpha Centauri's orbiting planet, Proxima b, back to earth. Breakthrough initiatives have identified four main challenges concerning the lightsail, the laser, the payload and the integration of the lightsail and the payload to achieve this. This report will focus on the design of the lightsail. An illustration of the lightsail can be seen in Figure 2.1.

For contextualization, the spacecraft that has travelled the furthest among human-built machines so far (NASA, n.d.) was launched in 1977 and is still collecting data after travelling more than 22 billion kilometres. After travelling for over 44 years, this spacecraft (Voyager 1) has only covered 0.5% of the distance to Alpha Centauri. Reaching Alpha Centauri with current technology seems unfeasible. Recent initiatives involving concepts similar to the lightsail are starting to show the potential of this idea. An important example is spacecraft IKAROS, which has an approximate 200 m^2 solar sail consisting of a thin polymer layer with a reflective metal coating. This spacecraft accomplished a successful mission in 2010 (Jaxa, n.d.). It should be noted that the design restrictions for solar sails are less strict than for lightsails because solar light has less power than the proposed laser used for a lightsail, allowing materials like polymers and metals (i.e. materials with high optical absorption coefficient). Section 2.2.4, elaborates on possible

choices for sail materials. However, for the lightsail concept proposed in the Starshot initiative a few standard parameters are set. These parameters can change in a later development stage, but they provide a good guideline for the design requirements. First, the mass constraint for both the sail and the satellite chip is 1 g. Secondly, the sail should be around 10 m^2 and should be propelled with a 10-100 GW earth-based laser. At last, the laser should use wavelengths in the near-infrared spectrum from 1 - 1.5 μm (Atwater et al., 2018).

2.2. LIGHTSAIL DESIGN CHALLENGES

A lightsail needs to be designed and constructed. This report only focuses on the design of the lightsail, but it is essential to understand the basic principles behind it. A lightsail can be fabricated on earth, but it needs to be transported into orbit. Consequently, it needs to be strong enough to survive this flight. When the sail is put in orbit, it needs to morph into its operating shape, after which a high power stationary laser can propel it. The light pressure generated by the laser on the sail will generate a force large enough to accelerate it. From this point on, the lightsail should be propelled in the right direction without going off course. Inevitably, some of the energy of the laser will generate heat in the sail. Furthermore, the lightsail can encounter all sorts of space debris or radiation during flight, which should not result in structural failure. Thus, it can be concluded that the lightsail should overcome many complex challenges starting from manufacturing to successfully reaching alpha Centauri in one piece. Strict design criteria need to be set regarding mass, reflectivity, thermal management, flight stability and flight resilience are required to achieve a high-performance lightsail. Some of these challenges can be solved by proper material choice, whereas other requirements can be met using design choices. A more detailed account of these design challenges is given in the sections below.

2.2.1. TRADE-OFF BETWEEN MASS AND REFLECTIVITY

The force that accelerates the lightsail is a function of the reflectivity and the area of the lightsail. The easiest way to increase reflectivity is by using a material with high refractive index (n). Additionally, the mass of the whole construction should be low for the generated force to be sufficient. This can be done by finding a material with low mass density. When following the Starshot parameters (i.e. a lightsail with an area of $10m^2$ and a mass of 1 g), the critical area density is $\rho_c = 1x10^{-4}\ kg/m^2$, which results in a sail of approximately 100 atomic layers thick (Breakthrough Initiatives, n.d.).Therefore, a trade-off between reflectivity and mass is required. A proper objective function (figure of merit) that translates this trade-off has been proposed in the literature as the acceleration distance of the sail (Atwater et al., 2018). The acceleration distance is the distance required to accelerate the sail from start to end velocity. As the sail accelerates, the perceived wavelength of the laser on the sail will Dopler red-shift (i.e. become larger). This is an important factor to consider because this means that the sail should be highly reflective over a large bandwidth. The acceleration distance is presented in Equation (2.1).

$$D = \frac{c^3}{2I}(\rho_l + \rho_s)\int_0^{\beta_f} \frac{h(\beta)}{R[\lambda(\beta)]}\, d\beta \tag{2.1}$$

Where D is the acceleration distance, I is the intensity of the propulsion laser, ρ_l and ρ_s are the area densities of the lightsail and the satellite respectively, λ is the wavelength of the propulsion laser, R is the reflection as a function of λ. $h(\beta) = \beta/(1-\beta)^2\sqrt{1-\beta^2}$ in which beta is the velocity fraction with respect to the speed of light $\beta = v/c$. Due to the Dopler red-shift of the laser, the wavelength of the laser can be written as a function of the relative speed, $\lambda(\beta) = \lambda_0\sqrt{(1+\beta)/(1-\beta)}$. When following the standard Starshot parameters, the bandwidth at which the sail should operate is from 1.2 μm to 1.44 μm.

Despite the acceleration distance being an important figure of merit, it does not consider acceleration forces. A fast acceleration could result in structural failure of the sail. At a later stage, this should be considered as well.

2.2.2. FLIGHT STABILITY

Complete control of the lightsail trajectory is required in order for the lightsail to reach its final destination. In literature, multiple solutions are proposed to ensure this control, as presented in Figure 2.2. One way of increasing the lightsails stability is by changing the shape of the sail. The lightsail is often depicted as a square flat surface but in Schamiloglu et al., 2001 a conically shaped sail is proposed, which ensures a carbon radiation (i.e. microwaves) to keep following the trajectory of the laser (Figure 2.2(1)). A more novel solution to this problem is proposed by Salary and Mosallaei, 2020 and Ilic and Atwater, 2019. Both articles describe the design of a nanophotonic meta grating that enables a stable fight. This metagrating is designed in such a way that there is a restoring force generated by the sail when submitted to small perturbations (Figure 2.2(2)). Notably, not only the sail itself can be changed to increase flight stability, but also the laser can be changed for this purpose. Myilswamy et al., 2020 proposed an alternative approach in which the non-uniform response of a 2D photonic crystal (PhC) is tuned to obtain an equal reflection over the sail, thus establishing that no distorting forces can occur. A hybrid of these ideas is proposed by Manchester and Loeb, 2017. In this paper, a curved sail design is proposed with a laser having a non-uniform intensity distribution. The sail can be trapped and controlled by using both a spherical lightsail, as well as a non-uniform laser intensity, characterised by a high to low intensity from the outside to the inside of the laser beam, (Figure 2.2(3)). It should be noted that these studies are all theoretical and non of them take the production or operating conditions into account. For example, these studies assume the sails to be flat, which will not be the case in operating conditions unless the sail is tensioned. The sail will be bent by the force generated by the laser and could eventually break due to the bending. In conclusion, the feasibility of these designs needs to be studied before considering these novel shapes.

2.2.3. HEATING

The energy absorption of the lightsail becomes a significant concern when accelerating the lightsail with a high-intensity laser of 10 GW. This energy absorption will result in heating of the sail, and thermal stresses or temperatures that reach the maximum operating temperature can cause material failure. A material with low optical absorption (α) is needed to prevent this. There are two ways the lightsail can lose its heat, both by black body radiation and by conducting the heat to the main structure holding the sail (Atwater et al., 2018). The black body radiation will be the largest source of energy

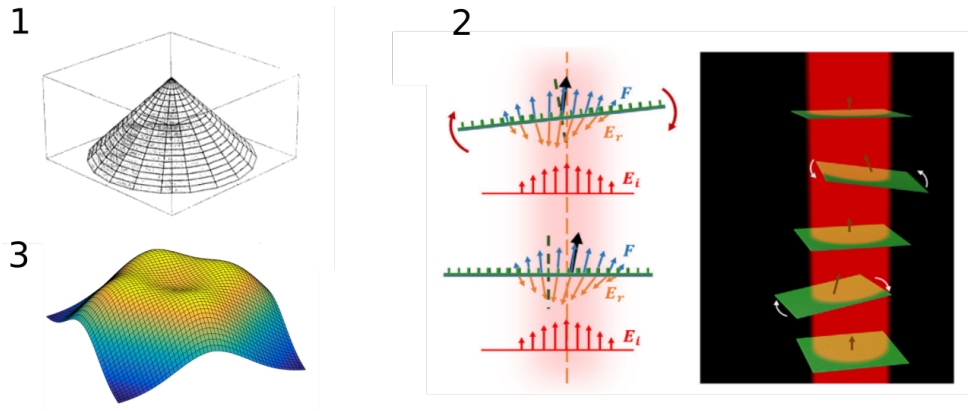

Figure 2.2: Proposed solutions to create flight stability in a lightsail. (1) A conical shaped sail proposed in Schamiloglu et al., 2001. In (2) the working principle of a lightsail with a meta-grating is shown. With a small perturbation, a restoring force is created (Salary and Mosallaei, 2020). (3) shows the non uniform intensity distribution proposed in Manchester and Loeb, 2017 to 'trap' a spherical lightsail.

loss. Therefore, a material with high emissivity (ϵ) in the infrared spectrum is needed to increase the black body radiation. Although the obvious solution would be finding a material with low α and high ϵ, other solutions are also proposed in the literature. In Ilic et al., 2018 a hybrid approach is used. A Si layer is used on the incident side of the sail because of its low optical absorption. At the rear side, a SiO2 layer is used because of its high emissivity. By tuning the thickness of the layers, the desired equilibrium temperature is obtained. Another way to influence the heating of the sail is by the photonic design. In Salary and Mosallaei, 2020 a study regarding a sail with PhC pillars on top of it is performed. It is shown that the diameter of the pillars influences the equilibrium temperature of the sail. The factors mentioned above are all regarding the sail design. One last cause of thermal failure of the sail could be the production process of the sail itself. Residual material left from the production process with a much higher optical absorption coefficient can create hot spots and result in failure (Norte and Groblacher, 2021). New production techniques, which will be discussed in section 2.3, need to be developed to prevent this.

2.2.4. MATERIAL

The previous sections identified four key design considerations for lightsails, allocated to 4 material properties: density, refractive index, optical absorption and emissivity. This shows that the material selection for the lightsail is a crucial component in the design process. The optical absorption controls the heating caused by the energy of the laser that is propelling the sail. Low optical absorption is required to reduce material heating. Therefore, metals with high reflectivity cannot be used. Metals have too much absorption from free carriers (Atwater et al., 2018). An aluminium coating could be used on the sail in the IKAROS project because it used sunlight as a radiation form with much lower power than the required land-based laser needed for the lightsail. Contrary to metals, semiconductors have a high refractive index and low absorption. This is possible be-

cause they have refractive indices just below the band edge energy transition (Atwater et al., 2018). The disadvantage of these types of semiconductors is the relatively high mass density compared to metals. Only a thin film of around 100 atomic layers thick can be used to comply with the mass constraint (Atwater et al., 2018). As a comparison, the IKAROS sail is 7.5 μm thick. Nanophotonic structures on the sail are required to achieve high reflectivity for these thin layers. There are many nanophotonic structures ranging from 1D PhC consisting of stacked materials with different material properties to 3D PhC's consisting of intricate sub-wavelength sized design features. However, only 2D PhC (i.e. planar structures with periodic designs) can comply with the density constraint. Possible PhC designs for lightsail use will be discussed in section 2.4. For the refractive index and emissivity, there is less of a trade-off to be made. These must be as high as possible.

A lot of suitable materials are proposed in the literature. A list of the promising materials is presented in Table (2.1). As described in section 2.2.3, a multi-material sail using SiO_2 in combination with Si is proposed in Ilic et al., 2018. Following Atwater et al., 2018 the two candidate materials are MoS_2 and crystalline silicon (c-Si) due to their high refractive index and low mass density and absorption coefficient. A material which is not often mentioned in literature is Si_3Ni_4, but Moura et al., 2018, and Wentzel-Long and Landis, 2020 propose this material due to its low absorption, high ultimate tensile strength and high internal stress, which would result in a relatively flat sail. In addition, Hoang and Loeb, 2017 considered a material that is not a semi-conductor, graphite , that due to strength can potentially address factors like space debris collisions, solar winds and structural integrity. In Table 2.1 the material properties mentioned above are overviewed.

Table 2.1: Material properties of potential lightsail material. n is the refractive index, ρ is the density, α is the absorption coefficient

Material	n [-]	ρ [g/cm^3]	α [cm^{-1}]	
Si_3Ni_4	2.0	3.2	10^{-6}	X. Chen et al., 2017, Abedrabbo, 1998
SiO_2	1.4	2.3	10^{-6}	Ilic et al., 2018, Salary and Mosallaei, 2020
Diamond	3.1	3.5	0.02	Atwater et al., 2018
c−Si	3.8	2.5	0.02	Atwater et al., 2018
a−Si	3.5	2.5	1	Atwater et al., 2018
MoS_2	4.5	4.8	3	Atwater et al., 2018

Note that other factors like availability, producibility and scaling need to be considered in the material choice as well. These factors are highly dependent on the upcoming technological developments. Firstly, the material should be suitable for producing a large scale PhC given the size of lightsails. Si_3Ni_4 is the only material that has been used to fabricate at the centimetre scale and has a reflectivity greater than 90% at the critical density (Moura et al., 2018; Norte et al., 2016). Secondly, almost all the PhC's are designed as flat sheets with high reflectivity for a normal incoming light beam. These designs will lose performance when the sail is not flat during operation. Si_3Ni_4 is a material that will not wrinkle during operation due to the internal stresses generated in the production. At last, the benefit of having an amorphous material like Si_3Ni_4 should not be overlooked.

An amorphous material does not tend to break over given crystal directions when subjected to stresses during operation, making it less prone to fail. For now, Si_3Ni_4 seems to be the material with the highest potential because the material has one of the best material properties as shown in Table 2.1 and performs the best under realistic conditions, as discussed above.

2.3. PRODUCTION METHODS

One topic not often addressed in the literature is the potential production method for the lightsail and its constraints on the design. As stated before, the lightsail would need to be in the range of 100 atomic layers thick. The feature size on the lightsail, when considering a 2D PhC pattern, can vary from 600 nm for a square lattice with holes, to features smaller than 100 nm for topology optimized structures. With these scales in mind, only nanofabrication methods would be sufficient for the production. The production can be divided into two parts: the production of the substrate material and the fabrication of the photonic pattern. Following the Starshot parameters, the lightsail should be around 10 m^2. For nanofabrication, thin plates of dielectric material called wafers are used. The largest wafers produced today are 450 mm in diameter (F450c, n.d.), which is equivalent to 0.16 m^2. One way to use them is by making a lightsail consisting of multiple panels, although this would lead to added weight to the system due to the extra structural elements needed for the panel mounting. For the lightsail to become feasible, larger wafers may be required to make a mass efficient structure. The fabrication of nano-sized patterns can be done in many ways. The most readily available technology used for this is lithography and etching. The basic principles behind this fabrication method work as follows. First, a substrate material is covered with a photoresist. A photoresist is a fluid that solidifies when exposed to a specific type of radiation (e.g.: uv-light, laser-light and electrons). After which, the radiation source illuminates the substrate with the required pattern, followed by rinsing the substrate that results in a pattern of hardened photoresist on it. The photoresists form a protective layer for the etching step, which creates the desired pattern. After etching, the photoresist is removed, resulting in a substrate with the required pattern (Z. Zhang et al., 2018). A schematic of this process is presented in Figure 2.3. The limiting factor for this production method is the lithography step. The source of radiation affects the minimal feature size and the speed of the process. Lithography methods can be divided into two categories, one using direct writing and the other using a mask. When using the direct writing technique, the process is similar to that of a laser printer. A focused beam illuminates one pixel of the design and creates the desired pattern by scanning the surface. The time it takes for the photoresist to harden depends on the beam's energy and the type of photoresist used. The minimal feature size depends on the spot size, which can be created for a specific beam type. This process can be accelerated by using a mask. A mask is a glass plate on which a thin metal layer with the desired pattern is made. This way, a substrate covered with a photoresist needs to be illuminated only once to create the whole design patterned. The disadvantage of these masks is that they are expensive, which makes them only suitable for mass production (Franssila, 2010). When producing large areas of nanopatterning for the lightsail, both the resolution and the speed of the production method need to be considered. The resolution is the smallest feature size which can be made with high fidelity. The throughput

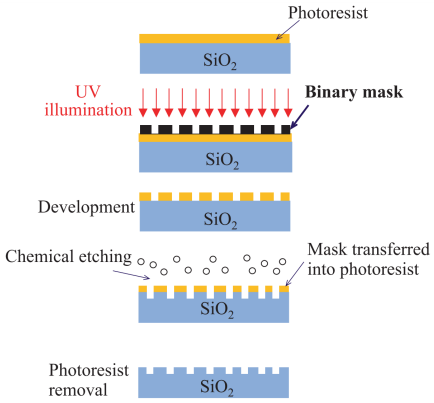

Figure 2.3: Schematic representation of a regular photolithography and etching process (Z. Zhang et al., 2018)

Table 2.2: The Resolution, speeds and relative costs of commonly used lithography methods in industry. Electron beam lithography (EBL), focused ion beam lithography (FIBL) and laser lithography are presented with a mask-less (ML) variant (Hasan and Luo, 2018).

lithography method	**resolution [nm]**	**Throughput**	**Costs**	**literature**
ArF laser (optical)	>200	>250 wafers/hr	medium	Bolk, 2020
(ML) ArF laser	>500	>80 wafers/hr	low	Z. Zhang et al., 2018
(ML) EBL & FIBL	<5	40 wafers/hr	high	Hasan and Luo, 2018
Extreme ultraviolet	<10	>150 wafers/hr	very high	Hasan and Luo, 2018

is used as a comparison metric for speed. This metric is the number of wafers that can be exposed per hour. In Table 2.2 an overview is presented of different lithography methods with their respective minimal feature size and speed. In addition, any radiation source can be combined with a mask. With the use of a mask, around 10^{10} pixels per second can be created, which is much faster than direct writing of all the pixels.

As stated in section 2.2.3 the production method can influence the performance of the lightsail. Traditional wet-etching methods tend to leave residual dried liquid on the substrate after the etching step. These dried etchants have different properties and can cause heating or reflectivity loss (Norte and Groblacher, 2021). A more recent approach is the dry-etching method. This technique is based on using chemical vapours or plasma for etching the material. This procedure results in a clean substrate and is therefore an attractive alternative for the wet-etching method.

Currently, the lightsail design is not advanced enough to make a proper decision on the best production technique. It should be noted that the following statements are made with the consideration that nano-sized features are required in the design of a lightsail. For a large sail, it could be beneficial to make one mask and scan the whole sail using this mask. This approach would reduce the production time and making the sail less prone to machining errors. Furthermore, this approach would drastically reduce the price for large areas compared to direct writing. However, the use of a mask would not be beneficial at the prototyping stage, in which a lot of different testing samples need to

be produced rapidly. For this purpose, direct writing by laser beam lithography would be ideal due to the process simplicity, cost, and speed. The disadvantage of this method is the large minimum feature size, but this can be considered when designing the PhC. On the other hand, electron beam lithography would be suitable when a small feature size is required. The biggest drawback of this technology is the requirement of a vacuum chamber, which could be problematic when scaling to meter-sized wafers. Furthermore, the price for producing a large area with nano-sized features is high with this method. At this moment, Additional conclusions cannot be made, and more research needs to be done on the final production methods concerning the sail's sizing and structural design.

2.4. DESIGN SOLUTIONS PROPOSED IN LITERATURE

As stated in section 2.2.4, the lightsail consists of a nanometer-thin film with a nanopattern to provide sufficient reflectivity and low mass. In literature, it is shown that photonic crystals can create thin and large bandwidth reflective materials. Although these publications are not all based on designing a lightsail, they provide an overview of the PhC's high reflectivity capabilities. In different designs, there is often a trade-off between thickness and bandwidth. An overview of the different designs discussed below is presented in Figure 2.4. An average of 98% reflectivity over a 200 nm bandwidth is achieved by Moitra et al., 2014, by making 500 nm large Si pillars on a 2 μm SiO_2 substrate (Figure 2.4(1)). For a lightsail, the material should be as thin as possible to reduce mass. In Norte et al., 2016 and Bernard et al., 2016 it is shown that a thin (<60 nm) layer of Si_3Ni_4 with a 2D photonic crystal pattern on it can provide 99% reflectivity at a desired wavelength. In both studies, sub-wavelength sized holes in a square lattice pattern and a Si_3Ni_4 substrate are used (Figure 2.4(3)). The downside of these results is that the bandwidth is limited. Additionally, a computational study presented in Harper et al., 2020 designed a PhC structure made of 502 nm Si pillars on a SiO_2 substrate, which has a reflectivity of 99% over a bandwidth 450 nm, centred around a target wavelength of 1550 nm. Notably, this study is purely computational, and some physical parameters like substrate thickness are not provided. Therefore, experimental tests need to be done to check the validity of these results. Previously, literature has shown the potential of using PhC's for high reflectivity applications. So far, several papers have already described design solutions specifically for a lightsail. However, the design feasibility is often overlooked. Some high reflectivity PhC's are manufacturable and straightforward but are not optimized for a lightsail. Others have optimized designs but consist of complicated and non-feasible structures. A good example of an unfeasible design is presented in Jin et al., 2020, in this study, a unit cell for a lightsail is explicitly optimized for the Starshot parameters (Figure 2.4(2)). These optimized structures consist of thin nanobeams and floating (i.e. not connected material) 2D PhC's. Scaling these nanobeam unit cells to a full-scale lightsail increases the probability that they will collapse or stick to each other considerably. Although more investigation needs to be done on enforcing producibility in this paper, it shows the great potential of using topology optimization for complex nanophotonic design. However, some articles like Moura et al., 2018 propose manufacturable designs. This design 2D PhC consisting of subwavelength holes following a square lattice is similar to the design in Norte et al., 2016. However, this design is not optimized for a lightsail because it has a high reflectivity at one specific wavelength instead of over the desired

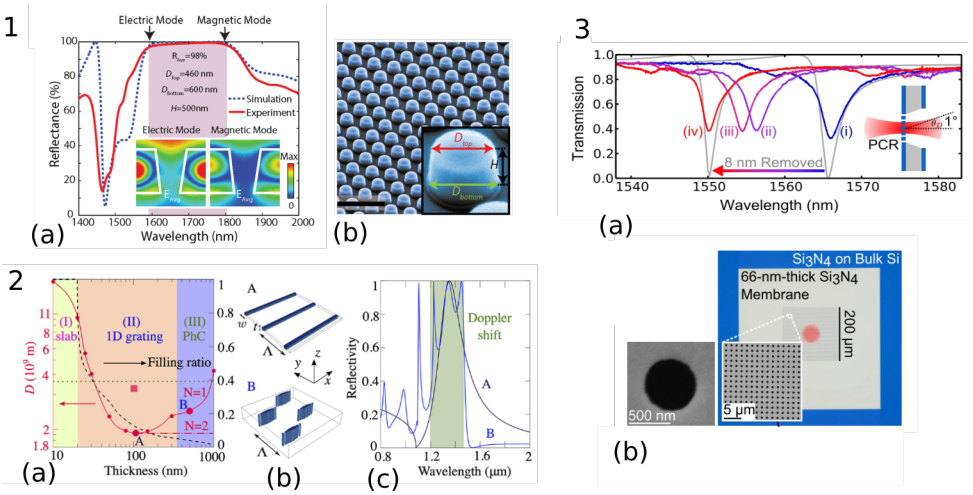

Figure 2.4: Performance of different photonic crystal designs. (1) shows the reflectivity(1a) of the design(1b) presented in Moitra et al., 2014. (2) represents the optimisation performed in Jin et al., 2020. (2a) shows the optimal values found the acceleration distance (D) for optimizations with different thicknesses. Two optimized results are presented in (2b) from which their reflectivity is plotted in (2c). The Transmission of different sized holes (3a) for a square lattices (3b) is presented in (3) (Bernard et al., 2016).

propulsion spectrum. Strikingly, barely any attention was given to the structural design of the lightsail in literature. Better design methods need to be developed which can enforce the strict design requirements for the sail. At last, it should be noted that the least researched topic for the lightsail is the shape and functionality of the structural support of the sail. Certainly, the extra mass that it would bring will largely impact the correct figure of merit needed for an optimal design.

SEARCHING FOR THE OPTIMUM DESIGN

For now, the design of the lightsail is far from being optimized for its final application. Therefore, it is unknown what is the optimum design for a lightsail. In the previous sections, different operational conditions were discussed. The acceleration distance is an easy to implement objective, but this is not the only important consideration. The sail should be optimized to deal with the sail's heating, and the sail should not break due to the acceleration forces. At last, the sail should be manufacturable. Optimizing manufacturability could result in a sail with larger PhC features, although this is not beneficial for the other design constraints. Besides the acceleration distance, manufacturability will be the report's focus because a manufacturable design would allow testing and validation in the lab. The proposed design constraints are challenging to implement and require a suitable design methodology.

2.5. CHALLENGES IN THE DESIGN PROCESS

Traditionally, the design processes for nanophotonic devices are highly iterative. Desired characteristics are obtained by changing the parameters of a design with a known phys-

ical effect. This methodology led to a large number of standardised devices with known behaviour. These devices are suitable for standard controlled applications but fall short for more complicated applications, for which nonlinear or multi-frequency behaviour need to be considered (Jin et al., 2020). Notably, new designs are only proposed by scientists with years of experience in the field. The following three problem characteristics make the design of a nanophotonic device time consuming and non-intuitive. First of all, nanophotonic devices are high dimensional. Therefore many design variables can have a significant impact on the performance. Secondly, the nanophotonic devices performance analysis cannot be performed analytically, requiring computationally heavy algorithms instead. Lastly, the design problem is non-unique, which means that multiple designs can have the same performance (Z. Liu et al., 2018). At the start of the design process, a design parameter sweep is often used to get an overview of the design parameter sensitivities with respect to the performance. The drawback of this method is that it is often a manual optimization approach which is inefficient for large design spaces. For intricate designs computational optimization techniques are required (Campbell et al., 2019).

In the nanophotonics field, the method of inverse design has gotten more interest in the last years. Inverse design allows the input to be the desired performance parameter (e.g., transmission or reflectance spectrum) and obtain an optimal design for this metric. A large design space can be considered using this method. Thus photonic devices can be designed close to their performance limit, reducing the experimental design effort drastically (Molesky et al., 2018). Optimization algorithms are an essential part of the photonic inverse design algorithm. Whether an algorithm is suitable for a specific problem is dependent on the number of input parameters, the number of objectives and the function cost evaluation. Several computational expensive analysis methods are often used to evaluate the photonic designs, such as Finite Element Method (FEM)(Nikishkov, 2004), Finite-Difference Time-Domain (FDTD) (Archambeault et al., 2012.) and rigorous coupled-wave analysis (RCWA) (V. Liu and Fan, 2012).

The FDTD is an easy to implement numerical method that solves the Maxwell equations directly. This method is volume-based and thus requires a uniform mesh. The problems are solved in the time domain, allowing it to compute time-dependent problems (e.g. transient behaviour). The FEM is a numerical method that can approximate partial differential equations (PDE). The PDE is approximated by combining the solution of all the nodes for the discretised design space. Complex functions can be approximated with high precision by using many elements.This method is mainly used for steady-state problems. This method can describe complex geometries as the mesh shape is flexible and can be non-uniform. The RCWA is a computationally efficient semi-analytical method to solve scattering problems for 2D periodic structures invariant in height. The structures can consist out of multiple layers with varying thicknesses. FEM and FDTD can be used in more general cases than the RCWA, and they can both be extended to solve 2D and 3D problems.

2.6. TOPOLOGY OPTIMIZATION

Topology optimization (TO) is an optimization approach that is suitable for inverse design. This optimization technique allows for innovative non-trivial designs because it

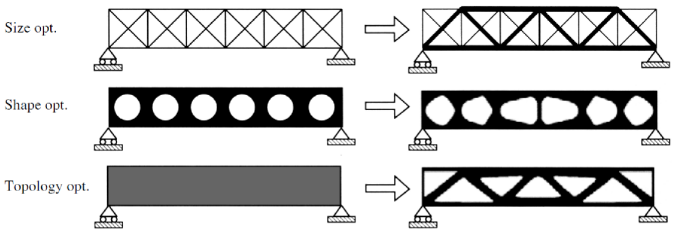

Figure 2.5: Examples for TO approaches used in structural design. (a)size optimization, (b) shape optimization, (c) free-form optimization, (Gebisa and Lemu, 2017)

redistributes material in a user-defined design space to achieve the desired behaviour (W. Li et al., 2019). In general, the approaches used in TO are size optimization, shape optimization and free-form optimization, as presented in Figure 2.5. In size optimization, the cross-section of members from a predefined structure are changed. For shape optimization the parameters of predefined shapes are optimized and in the case of free-form optimization the material distribution is optimized in a discredited design space (Gebisa and Lemu, 2017). In the nanophotonics field, shape and free-form optimization are mainly used. The advantage of shape TO is the relatively low computational costs compared to free-form TO because of the limited design variables. On the other hand, the advantage of free-form TO is the possibility of highly optimized and non-trivial designs since there are fewer constraints to the design space. In literature, both gradient-based (GTO) and non-gradient (NGTO) optimizers have been proposed to be used in TO. Only the objective function evaluations are used to find the optimal solution in the NGTO algorithms, whereas GTO uses the gradients of the design variables with respect to the objective function in the optimization process. Using these gradients often results in reaching an optimum with less objective function evaluations. Therefore, this makes the GTO computationally more efficient because the performance analysis (i.e., function evaluation) of the design is the most expensive part of TO (W. Li et al., 2019). However, the benefit of NGTO is that it is easier to implement because no gradients need to be calculated. A subset of the GTO algorithms proposed in the literature is solid isotropic material penalization (SIMP), level set (LS) and bi-directional evolutionary structural optimization (BESO). The most used NGTO is a genetic algorithm (GA) (W. Li et al., 2019). Finding a global optimum cannot be guaranteed when using GTO or NGTO due to the characteristics of the design problem being non-linear and non-convex. In order to create a feasible TO algorithm for nanophotonic problems only GTO's are suitable. At the moment, the proposed NGTO's are not sufficiently computationally efficient. Adjoint based models are proposed to ensure a computationally efficient way to calculate the design sensitivities (Jensen and Sigmund, 2011). These models are able to efficiently calculate the derivative of the functional value with respect to the model parameters (Giles and Pierce, 2000).

It should be noted that there are many controllable parameters in TO. When creating the problem, the design volume, the external influences, the discretization and material parameters can be controlled. The filters applied for post-processing, the func-

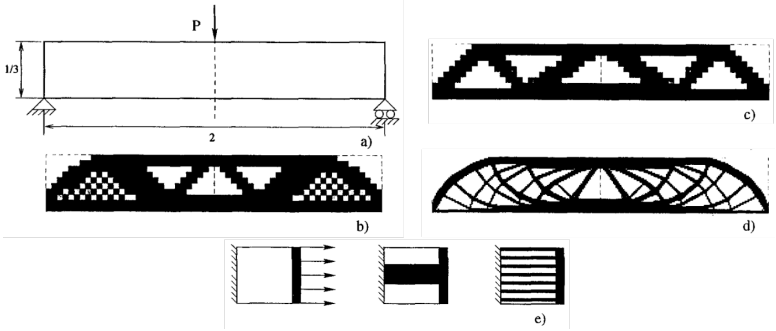

Figure 2.6: Problems regarding TO algorithms (Sigmund and Petersson, 1998). (a) The design problem, (b)example of the checkerboard problem, (c) solution of a course mesh optimization, (d) solution of a fine mesh optimization, (e) example of a non-unique optimization result.

tional analysis method (e.g. FEM), and the optimizer parameters can be changed to set up the optimization. Changing these parameters can have a significant impact on the outcome of the optimization. Many optimizations need to be performed with different optimization settings to find the best optimum. Besides this, checkerboard problems, mesh dependencies and the tendency to get stuck in local minima, which are presented in Figure 2.6, are three common problems that can be identified for TO algorithms (Sigmund and Petersson, 1998). Firstly, the checkerboard problem can be identified by a TO solution having material and voids close to each other in a checkerboard fashion (Figure 2.6(b)), which is in practise a non-feasible solution. Secondly, when changing the mesh size of the optimization the TO can result in a different structure, which results in a mesh dependent solution (Figure 2.6(c, d)). Notably, TO tend to create "spider web" like structures, consisting of thin connections, which are non-practical designs. At last, TO optimizations tend to get stuck at local optima because of the flatness of the objective function and the solutions are often non-unique ((Figure 2.6(e)) (i.e. different solutions with the same output). These problems can be mitigated by adding post-processing to the solutions (e.g. filters, patches) or changing the optimizer. These mitigation methods will not be discussed. It should be noted that TO is highly sensitive to its optimization parameters (Deaton and Grandhi, 2014).

2.6.1. PROPOSED APPLICATIONS OF TO IN LITERATURE

TO is already used for the design of a wide range of nanophotonic devices such as metagratings, waveguides and photonic crystals (Molesky et al., 2018, Jensen and Sigmund, 2011). A selection of these applications will be discussed below and are presented in Figure 2.7. One way TO is used for nanophotonic devices is for the optimization of the bandgap of materials. For example, a PhC can be designed to pass or block specific wavelengths. Larger band gaps often lead to broader available bandwidths of signals and applications. A free-form level set (van Dijk et al., 2013) TO algorithm is used by Kao et al., 2005 to maximize the bandgap of 2D photonic crystals. The level set TO is chosen as the solution is preferred to be piecewise-constant (e.g. creating a binary material-vacuum design). Using this method, they show the design of the largest bandgap for 2D

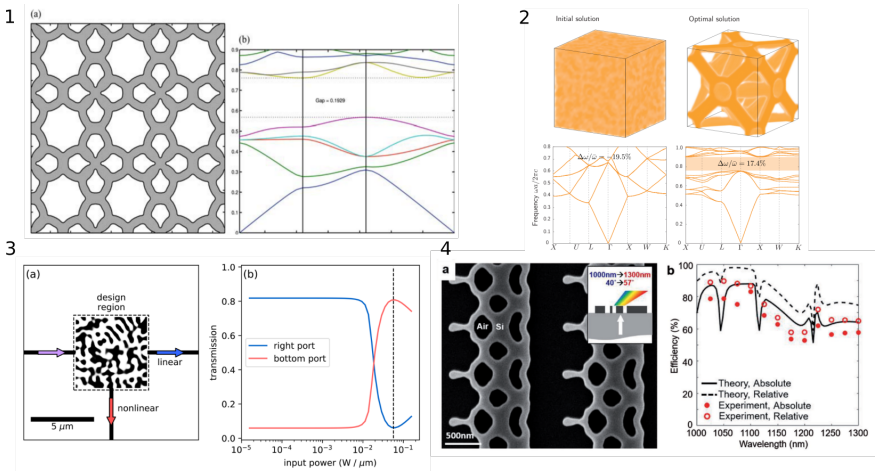

Figure 2.7: Examples from literature which use free-form TO. (1) shows the optimized structure(1a) of a 2D PhC from GaAs in air, with the objective to maximize the band gap between two desired bands(1b) (Kao et al., 2005). A similar approach is used in (2) for which the band gap is optimized for a 3D PhC (Men et al., 2014). A non-linear waveguide is presented in (3), the optimized structure (3a) results in direction change of the light for different frequencies(3b) (T. Hughes et al., 2018). An optimized metagrating (4a) which is able to change the angle of incoming light of different frequencies (4b) (Sell, Yang, Doshay, and Fan, 2017).

PhC at that time. However, they acknowledged that the designs are probably still local optima (Figure 2.7(1)). Men et al., 2014 proposed a free-form level set TO method that includes production limitations and considers 3D designs instead of 2D. Furthermore, new crystal symmetry constraints are implemented, which allow the consideration of more symmetry groups. In this paper, it is concluded that it is hard to improve existing designs significantly and that it is impossible to state if a global minimum is reached (Figure 2.7(2)).

For the design of waveguides, TO has proven to be effective as well. Waveguides are nanophotonic devices that can alter the direction of a light beam. A new non-linear adjoint model is proposed by T. Hughes et al., 2018 for the design of nanophotonic devices. They were able to design a new compact optical switch with Kerr non-linearity (Figure 2.7(3)). In this work, a general formulation to solve other non-linear 2D optical problems is presented. One year later, in T. W. Hughes et al., 2019, a new gradient-based inverse design TO is proposed, which uses the forward-mode differentiation (FMD) method for Maxwell's equations. It is shown that the FMD could be an alternative for adjoint-based models for problems with more outputs than inputs because the FMD has to run separate simulations for the inputs and the adjoint model for the outputs. As a result, the FMD has improved memory and speed scaling for these types of problems. In the last years, the development in the inverse design TO methods is progressing fast. A nanophotonic design platform was proposed in Su et al., 2020 to facilitate the use of these new developments. The framework allows using small building blocks to create optimizations. Furthermore, much documentation is provided to help apply the proper optimization parameter. The platform's main goal was to allow designers to design devices and test

for different objectives quickly.

The design problem of a light sail is similar to that of a metagrating. The goal of a metagrating can range from bending and reflecting the light to changing the light's polarisation. In general, metagratings are 2D shapes with a fixed height for which the incident light is normal to this surface or with an angle with respect to the normal of the plane. In Sell, Yang, Doshay, and Fan, 2017 and Sell, Yang, Doshay, Yang, et al., 2017 the potential of free-form TO for high efficient metasurfaces is shown (Figure 2.7(4)). RCWA is used as it allows for fast and accurate analysis of periodic structures. Their method optimizes wavelength-scale devices, resulting in complex designs and behaviour. Remarkably, the achieved performance exceeds that of current devices. In literature, free-form TO is also used for the of design broadband reflectors. A 2D PhC consisting out of different layers is optimized lightsail in W. Li et al., 2019. The gradient-based method of moving asymptotes (MMA) (Svanberg, 1987) is used for the TO method to cope with a large number of design variables. Furthermore, a free-form and adjoint-based TO approach are applied together with the RCWA. Notably, the performance of their designs is 50% better compared to other designs at the time. Notably, the publications presented above only state that their methods perform better than previous methods but do not explicitly explain why this is the case.

2.7. MACHINE-LEARNING ENHANCED TOPOLOGY OPTIMIZATION

An upcoming approach for the design of photonic devices involves the use of Neural Networks (NN), holding the promise of solving the drawbacks of traditional TO (Campbell et al., 2019). A NN is part of a larger group of computational algorithms called machine learning. Machine learning (ML) is an evolving field that tries to emulate human intelligence in computational algorithms.

2.7.1. MACHINE-LEARNING PRINCIPLES AND ARCHITECTURES

ML algorithms can be distinguished into three groups based on their learning methodology (El Naqa and Murphy, 2015). Learning can be defined as the process of estimating dependencies from data. The following groups can be distinguished: supervised learning, unsupervised learning and reinforcement learning. In supervised learning, the input data and corresponding outputs (i.e. label) are provided to an optimization algorithm that tunes the ML-algorithm variables to estimate outputs for unknown inputs. In unsupervised learning, known input data is provided without any corresponding label. This can be used to recognize similar patterns within data, called clustering. At last, reinforcement learning takes another approach. With this approach, no training data is required. Instead, the algorithm learns to operate in an environment by receiving feedback. For example, an agent is playing a game without knowing the rules of the game. The goal for the agent is to maximize the score for this game. The agent trains itself to play the game by repeating the game several times, getting feedback on his performance and changing its internal parameters accordingly.

Each of the learning methods described above can be implemented on a given ML architecture. A ML architecture is a certain implementation of a NN and will be discussed in the following section. Three main machine learning architectures are used for

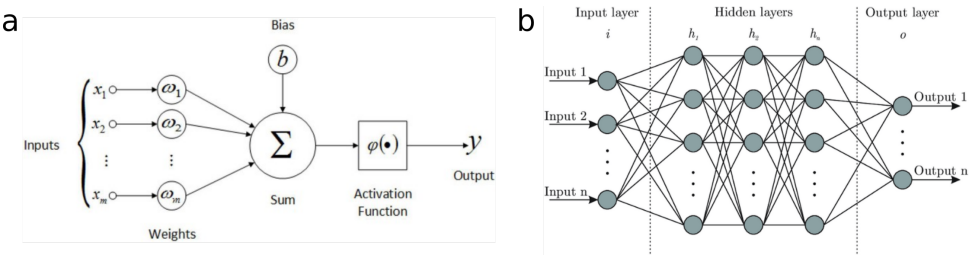

Figure 2.8: (a) Basic architecture of a perceptron. The three input's are multiplied by weights and added together. This weighted sum is fed through a activation function (step function) which has a binary output when a threshold is reached. (b) NN with 3 hidden layer (Martins et al., 2012).

the design of nanophotonic devices: fully connected neural networks (FCNN), convolutions neural networks (CNN) and generative adversarial networks (GAN). In addition, some papers propose more traditional machine learning algorithms like support vector regression (SVR) and decision trees, but these will not be discussed in this paper. The three main ML approaches named above are based on artificial neurons, which are inspired by biological neurons. An artificial neuron is a function that has one or multiple inputs and has one output with respect to these inputs. Together, these neurons can be combined to the smallest NN called a perceptron, presented in Figure 2.8 (Géron, 2019). As an analogy, one can see the perceptron as a weather prediction model, which has as input: humidity, pressure and temperature, and as output a one if it is going to rain and zero when the sun shines. This perceptron has learned at which inputs it will rain by feeding it available data from years before and changing its weights to get the required output. After this training procedure, it will predict the weather according to new inputs (e.g. unknown situation). Furthermore, these NN can be made more complex by adding more inputs, adding layers and adding a bias to these layers, which is presented in Figure 2.8. One can change the NN by changing the number of inputs, outputs, layers and the type of activation function. Eventually, during the learning process the weights and the biases are changed to reach the desired output. Finally, when all neurons are connected in a NN they form a fully connected neural network (FCNN).

NN's, as described above, can find complex relations between the input and output data. A significant disadvantage of these networks is that as the problem's complexity increases (e.g. image and voice recognition), the number of connections between the different layers will increase drastically. For example, analysing a picture with a regular FCNN, where the pixels of the picture are the inputs to the system, would inevitably lead to a large number of neurons and connections. On the contrary, a framework proven effective for these tasks is the convolutional neural network (CNN). A CNN takes another approach by pre-processing the image before it is fed in a regular FCNN, to reduce the number of connections. The essential building block of the CNN is the convolutional layer which applies a filter on the picture to extract high-level features from an image. The output of a convolutional layer is a new, filtered image with new features. Different image conversions (e.g. image sizing, called pooling layers) can be applied as well. However, these conversions will not be discussed. Notably, the main advantage of a CNN is the ability to extract high-level information from complex input data (Géron, 2019).

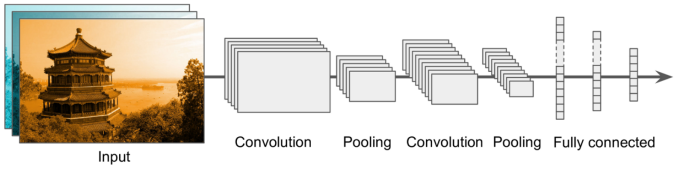

Figure 2.9: Basic architecture schematics of a CNN consisting of an image input with a convolutional and pooling layers, inserted into a fully connected layer (Géron, 2019).

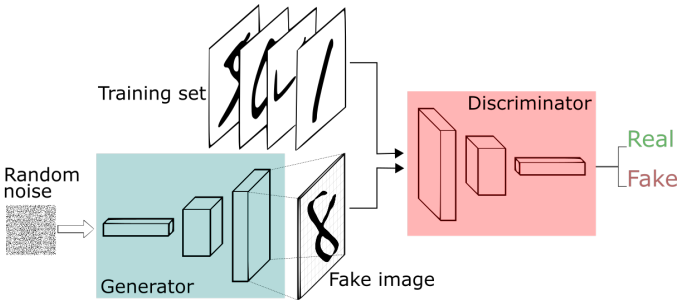

Figure 2.10: Conventional architecture of a GAN (Y.-Y. Chen, 2018), consisting of a generator which creates new images from random noise and a discriminator which tries to identify the new images as fake or real.

The schematic of a standard architecture of a CNN is presented in Figure 2.9. Lastly, the often proposed approach in the literature is a generative adversarial network (GAN). This network is mainly used to generate new images or structures. A GAN uses a generative and an adversarial model that works in competition. The adversarial model, also called discriminator, is trained to recognize the difference between new data created by the generative model and actual training data. The schematic of a conventional GAN is shown in Figure 2.10. This model can be compared to a team of counterfeiters (i.e. generator) trying to generate fake banknotes and the police (i.e. discriminator) trying to recognize the fake banknotes. In the end, the competition between the counterfeiters and the police leads to indistinguishable banknotes (Goodfellow et al., 2014). The generator and discriminator of the GAN are often made out of a CNN.

2.7.2. TRADE-OFF BETWEEN DIFFERENT ML APPROACHES

Having discussed the three most used ML architectures, we can now focus on their characteristics and benefits. NN's can be used for different goals. One goal is to change the use of computational resources. When a NN is appropriately trained, it can produce an output with significantly less computational effort than other non NN based methods (Campbell et al., 2019). Supervised learning methods can be used to train a NN. However, this requires a computationally expensive process that needs many training data. This training is done before the actual use of the NN, this way the computational effort is switched from an online process to an offline process which can be done beforehand. An offline process refers to training the algorithm before it can be used for its intended purpose, and the online process is the work the finalised algorithm performs to com-

plete its objective. Another benefit of using NN's is the ability of the algorithm to learn relations at different abstraction levels, which can lead to better performance or a more generalized solution (Campbell et al., 2019). This benefit is mainly exploited in the proposed CNN based or unsupervised algorithms. However, a disadvantage of NN is that often these algorithms do not obey physical principles. The designs generated by the NN are not governed by equations that find their basis in nature. Therefore, it is often difficult to enforce these equations in the process.

The different NN architectures discussed above are applicable in different contexts. A FCNN can be suitable for approximating complex physical problems because it can find the global optimum easier than traditional TO as a result of the smoothed design space (Peurifoy et al., 2018). However, the disadvantage of the FCNN is that the amount of variables increases fast for more complicated problems. Therefore, FCNN is mainly helpful for shape optimization with fixed parameters. On the contrary, the CNN has proven successful for problems that require the recovery of high-level details. By changing the convolutional layers, one can control the amount of detail taken into the model. Notably, a CNN is overly complex for small problems that can be converted to parameter optimization. Alternatively, a GAN can be used by training a CNN to generate new realistic data, often images. With in a GAN two CNN's are embedded (i.e the generator and the discriminator). The benefit of this method is that it does not optimize its parameters directly from the training data set but changes it according to the outcome of the discriminator. This results in learning the underlying logic of the training set rather than copying it. This way, it is possible for the GAN to recreate new and unseen data. Nevertheless, the disadvantage of the GAN is that it is difficult to get a robust code, and it is hard to control or guide the images created by the GAN (Pinetz et al., 2019). Interestingly, a way to control the created images of a GAN is by implementing labels to the training data in a conditional Generative adversarial network (cGAN) (Mirza and Osindero, 2014). A cGAN makes it possible to provide the generative network with inputs for what it should generate. For example, in face reconstruction one could give the choice of male or female. These inputs form the conditions which the cGAN takes into account for creating the output. To conclude, choosing the right ML architecture depends on the problem characteristics and the required outcome.

Notably, an essential factor that is mainly overlooked in literature is the architectural search. How a study obtained a NN architecture and why it is a good architecture are often not answered. New studies often use NN that are proven to work in other publications (Szegedy et al., 2017). These NN are often suitable for general use but not tailored to the new application in which it is used. This often results in using a NN that is unnecessarily large, which can result in over-fitting (Sarle, 1996) and unnecessary computational cost (Szegedy et al., 2017). Additionally, the hyperparameters (e.g. filter and regularization parameters) used within the different layers of the NN can have a significant impact on the results (Y. Zhang and Wallace, 2016). A lot of experience and time is required to find the correct hyperparameters. Checkerboarding like artefacts can be the results of these hyperparameters (Odena et al., 2016). Thus, although NN's have shown outstanding performance on many occasions, obtaining the right architecture for a problem can be non-trivial and is often not discussed literature.

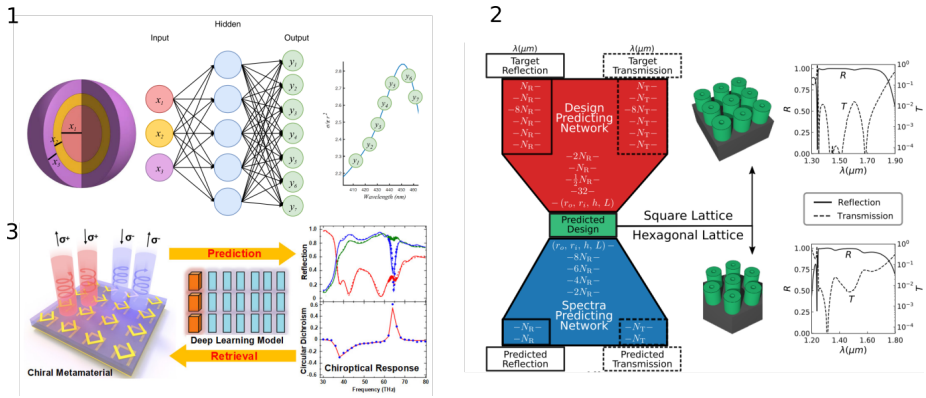

Figure 2.11: Examples using supervised learning in literature. (1) FCNN used to design the thickness of the layers with in a nano particle to obtain the scattering cross section at different wavelengths (Peurifoy et al., 2018). The schematic coding and decoding NN used for the parametric TO of nano pillars can be seen in (2) (Harper et al., 2020). (3) 3d chiral structures optimized for refelectivity by multiple connected NN (Ma et al., 2018).

2.7.3. PROPOSED SOLUTIONS IN LITERATURE

In literature, two approaches are used for integrating ML in TO. In one approach, the ML algorithm aids the existing TO by reducing the number of function evaluations or increasing the performance of the designed devices. In the second approach, the ML algorithm fully replaces the TO algorithm.

SUPERVISED LEARNING

Most of the ML algorithms used for inverse design are based on supervised learning (i.e. using labeled training data). Examples of supervised learning approaches for the inverse design of nanophotonic devices are discussed below and presented in Figure 2.11. For the inverse design of 1D nanoparticles, Peurifoy et al., 2018 proposes a FCNN that optimizes a particles geometry for the desired spectrum by changing the thickness of three different dielectric layers (Figure 2.11(1)). A similar approach is used in Malkiel et al., 2018, they propose a bi-directional NN consisting of two linked NN's. One NN predicts the geometry based on the desired spectrum, and the other predicts the spectrum based on a geometry. In the end, the NN is used for shape optimization of 2D nanoparticles. Harper et al., 2020 proposes a NN for the inverse design of a nanophotonic metasurface. A FCNN is used to optimize an all-dielectric meta-surface consisting of open cylinders. The number of design variables is reduced by applying a shape optimization in which only the parameters defining the geometry of the cylinders are optimized (Figure 2.11(2)). Interestingly, Ma et al., 2018 proposes a NN consisting of two bi-directional sub-NN's, which can predict a spectrum from a design and predict a structure from the desired spectrum. The NN performs a shape optimization for 3D chiral nanostructures. The whole NN consists of different decoding and encoding CNN's and conventional FCNN's (Figure 2.11(3)).

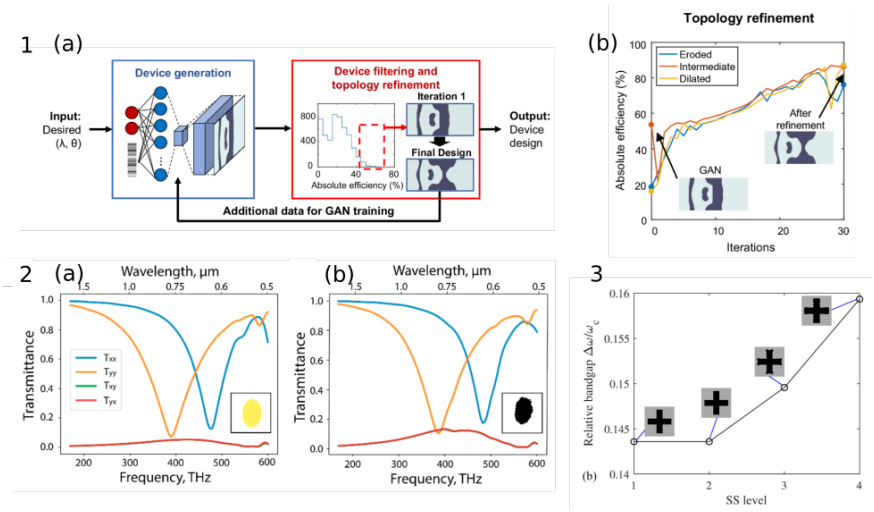

Figure 2.12: Examples using unsupervised learning for the inverse design of photonic devices in literature. The schematic of the approach used in Jiang et al., 2019 can be seen in (1a). (1b) The optimized structure generated in the GAN is further optimized with conventional TO. (2) Shows the prescribed spectrum (2a) which is fed into the GAN proposed in Z. Liu et al., 2018, and the obtained spectrum (2b) by the GAN. (3) The optimized structure after each Subset simulation presented in M. Li et al., 2021. The 2D PhC is optimized to maximize the band gap between two given bands.

UNSUPERVISED LEARNING

This section elaborates on examples from literature using unsupervised ML. Notably, these examples use data with out labels to train the network. The examples use figures of the nanophotonic devices as input data to train the network. In Jiang et al., 2019 a cGAN is used for the design of efficient metasurfaces (Figure 2.12(1)). The inputs for this network are, besides a vector with random numbers that provides diversity to the solution space, the operating wavelength and the deflection angle of the light. This makes the network a cGAN. This cGAN can generate new high-resolution and high-performance designs. The network is trained with designs created by a TO algorithm. The designs created by the trained cGAN are used as a new input for the TO algorithm to establish a final optimized structure. This way, the cGAN works as an addition to the design process by creating new and better performing designs than the original input. These designs are then further optimized to retrieve the full design potential. Also, in Z. Liu et al., 2018 a GAN is used for inverse design of metasurfaces (Figure 2.12(2)). The GAN can generate a structure that follows a prescribed spectrum with high fidelity. This approach allows for the generation of new metasurfaces without the user needing to have much experience in the field. The method proposed in M. Li et al., 2021 is based on a GAN as well. In this method, a subset simulation-based TO is proposed in which GAN-guided TO is used. The goal of the optimization is to maximize the bandgap of a 2D PhC. The efficiency and effectiveness are shown for 2D periodic structures with the use of this method (Figure 2.12(3)).

REINFORCEMENT LEARNING

Reinforcement learning-based approaches have not been proposed as much as the other two learning methods. Hoyer et al., 2019 proposes a reinforcement learning approach [1] that uses a decoding CNN for free-form structural topology optimization. The main idea is to use the "deep image prior" of a CNN, meaning they can perform tasks in image processing even before being trained, for structural optimization. The In Lempitsky et al., 2018 they show that untrained NN can capture high-level image statistics, which can be used for tasks like denoising in image processing. These deep image priors could be helpful in problems including spatial correlation, multi-scale features or translation invariance. Deep image priors are used in Hoyer et al., 2019 to re-parameterize structural optimization from a grid through a NN. The proposed NN is a decoding CNN for which the input vector is used as a trainable variable. The paper shows that optimization using the NN was faster and resulted in better optimized structures compared to traditional TO algorithms (e.g., method of moving asymptotes and optimality criteria). Another benefit of the approach is that it resulted in more general structures than traditional approaches, which generate spiderweb-like structures. A similar approach is used by Jiang and Fan, 2019 for the inverse design of a 2D metagrating. The algorithm used in this paper was able to find global optima. Furthermore, the performance of the generated devices is comparable with traditional adjoint-based TO algorithms. The main difference between Hoyer et al. (2019) and Jiang et al. (2019) is the goal of the learning procedure. In Jiang and Fan, 2019 reinforcement learning is used to optimize the NN to produce optimal structure based on targets that are set as inputs (e.g. wavelength and deflection angle). So, it is used to train the NN, which then can be used separately. In contrast, each optimization can be seen as a new optimization as proposed by Hoyer et al., 2019, in which reinforcement learning is only used to re-parameterize the optimization.

2.7.4. POTENTIAL IMPROVEMENTS USING ML-BASED TO

The ML-based TO is getting more attention because it can potentially solve the shortcomings traditional TO algorithms have. As stated in section 2.6, TO algorithms tend to get stuck in local minima. On the contrary, ML-based TO can potentially reach a global optimum in two ways. First, the ML-based TO can learn from past optimizations using supervised learning. Secondly, the optimization can reparameterize during the optimization when using a reinforcement learning approach as described by Hoyer et al., 2019. Another improvement ML-based TO can bring is the potential improvement of the post-processing of the optimized structures. The solutions from traditional TO can result in "spiderweb" structures due to mesh dependencies, which can be reduced by post-processing (e.g. filtering). However, in Hoyer et al., 2019 it is shown that their CNN results in more straightforward and general solutions. After having discussed many TO approaches, section 2.8 will discuss how to choose a suitable algorithm for the lightsail problem.

[1] The approaches used in Hoyer et al., 2019 can strictly speaking not be categorised as a reinforcement learning-based approach. However, they are categorised as reinforcement learning because they do not require training data like supervised and unsupervised learning.

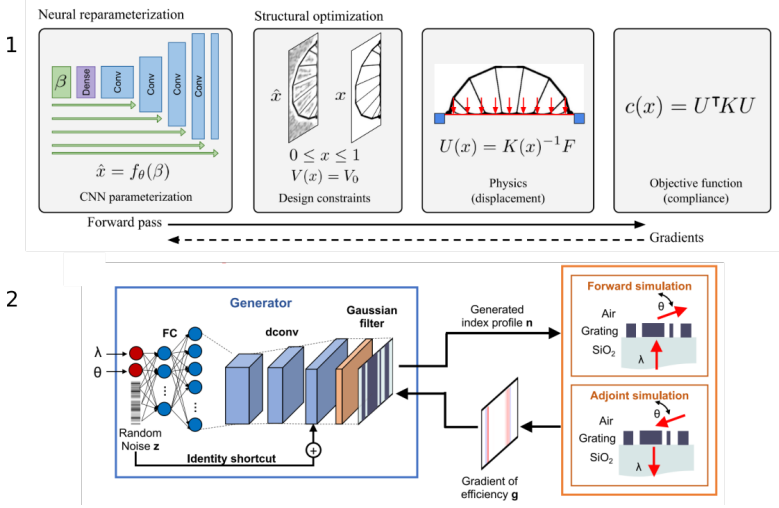

Figure 2.13: Examples of reinforcement learning used for TO in literature. (1) The schematic representation of the working principle used in Hoyer et al., 2019 fro which a decoding CNN is used for TO. In (2) the NN used in Jiang and Fan, 2019 to train a conditional model is presented.

2.8. CHOOSING A DESIGN ALGORITHM FOR A LIGHTSAIL

In the previous sections, different approaches for the design of photonic devices were discussed. In this section, the most suitable approach will be explained for the design of the 2D PhC used in a lightsail. First of all, it is important to take the problem characteristics into account when choosing the suitable optimization algorithm of a problem (Campbell et al., 2019). As stated in section 2.2.4, the lightsail design relies on a PhC design to achieve its performance. Therefore, large design spaces need to be considered to be able to create new and high-performance designs. Notably, most of the inverse design methods discussed above are suitable for this operation. Therefore, the question is, which method will perform the best for designing a lightsail. The first step is to find the suitable algorithm by using the flowchart proposed in Campbell et al., 2019. This flowchart contributes to find the best-suited optimization algorithm for nano-optical problems, Figure 2.14. Several characteristics need to be evaluated to use the flowchart for the PhC problem, like the discreteness of the input space, initial solution, time to perform a function evaluation and availability of training data. Ultimately, this results in two options: a deep neural network (i.e. when training data is available) and a surrogate model (i.e. when training data is unavailable). Deep learning algorithms that do not require training data, such as reinforcement learning based algorithms, are not included in the flowchart. However, recent literature has proposed these methods. Therefore, it can be concluded that the flowchart is not entirely up-to-date. This emphasizes that, although this flow chart provides a good direction for a suitable algorithm, other factors need to be considered when making a final decision between traditional TO-algorithms and ML-base TO. As shown in literature, there are traditional TO algorithms suitable for the inverse design of PhC. They are easy to implement and these algorithms are mature.

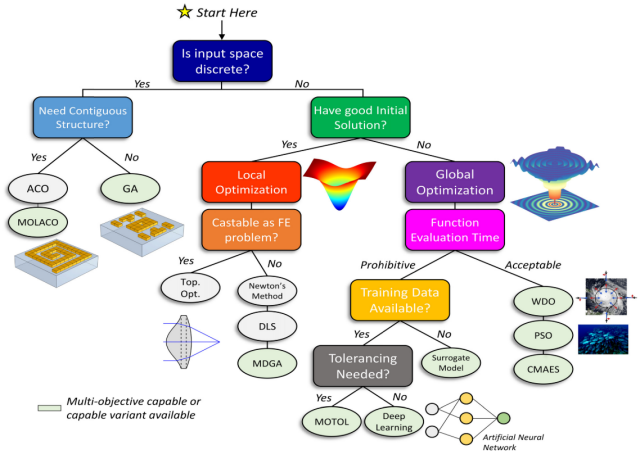

Figure 2.14: Flowchart proposed in Campbell et al., 2019 to find the suitable optimization method for nanophotonic devices.

However, traditional algorithms tend to get stuck in local optima, especially for photonic problems with highly fluctuating solution space. In addition, they are susceptible to optimization hyperparameters and they are computationally expensive because multiple runs with different initialization are required. On the contrary, the newly proposed ML-based algorithms have the potential to generalize (i.e. generate better or simpler structures) and have the ability to learn high-level information about photonic problems. However, there are also concerns regarding the use of ML algorithms in the field of TO. The novelty of the field creates uncertainty in the implementation and can generate unexpected results. Furthermore, most ML algorithms require large amounts of data to train. The last concern is that many ML algorithms do not use physical principles because this is often not enforced in the network. In section 2.9 the final trade off for a suitable the TO method for the lightsail problem is made.

2.9. SUMMARY AND CONCLUSION

Breakthrough initiatives have started the Starshot initiative to stimulate the design of a lightsail to reach Alpha Centauri within 20 years. A lightsails will be propelled by a high-intensity laser which is directed on the 10 m^2 sail. A highly reflective and nanometer-thin sail is required to achieve sufficient acceleration. A photonic crystal design is necessary to obtain high reflectivity and comply with the mass constrain. In literature, thin-film designs have been shown to achieve high reflectivity. However, non of the designs are suitable for a lightsail because they do not sufficiently consider operational conditions (e.g. manufacturability, flight stability and maximum heating). For a practical design, multiple objectives need to be combined to comply with all the operational requirements.

Literature has shown that traditional TO can be a valuable tool for designing nanophotonic devices. TO allows optimizing a large design space, which can result in highly optimized and non-trivial structures. However, there are still a few significant drawbacks

that can be improved. A significant disadvantage of the TO methods is that the optimizer can get stuck in local optima because TO methods are not global optimizers. Many optimizations with different initialization need to be considered to mitigate this, making it a time-consuming process. It is possible to use global optimization methods, although these algorithms often need to relax on physical accuracy (Campbell et al., 2019). Another disadvantage of TO algorithms is that they are computationally heavy and susceptible to optimization parameters, making it time-consuming to derive optimized structures. ML-based TO has proven to solve some of these problems and generate better and more general designs in less time. However, implementing these ML-based TO is a non-trivial process.

For the thesis, the ML-based TO approach as proposed by Hoyer et al., 2019 is applied to a lightsail. This approach has outperformed traditional TO algorithms for structural engineering and does not require any training. However, no equivalent topology optimization method has been implemented in photonics yet. It is expected that this method can result in a fast optimization algorithm and designs close to the global optimum compared to traditional topology optimization. Furthermore, the algorithms bias towards simple structures can result in producible PhC's. It is thought that the potential gains from this new method can drastically improve the design of the lightsail.

BIBLIOGRAPHY

Abedrabbo, S. M. (1998). *Emissivity measurements and modeling of silicon related materials and structures*. New Jersey Institute of Technology.

Archambeault, B. R., Ramahi, O. M., & Brench, C. (2012). *Emi/emc computational modeling handbook* (Vol. 630). Springer Science Business Media.

Atwater, H. A., Davoyan, A. R., Ilic, O., Jariwala, D., Sherrott, M. C., Went, C. M., Whitney, W. S., & Wong, J. (2018). Materials challenges for the starshot lightsail. *Nature Materials*, *17*(10), 861–867. https://doi.org/10.1038/s41563-018-0075-8

Bernard, S., Reinhardt, C., Dumont, V., Peter, Y.-A., & Sankey, J. C. (2016). Etch-tuning and design of silicon nitride photonic crystal reflectors.

Bolk, J. (2020). Arf scanner lithography for inp photonic integrated circuit fabrication.

Breakthrough Initiatives. (n.d.). Starshot [Accessed: 2021-03-29]. https://breakthroughinitiatives.org/initiative/3

Campbell, S. D., Sell, D., Jenkins, R. P., Whiting, E. B., Fan, J. A., & Werner, D. H. (2019). Review of numerical optimization techniques for meta-device design. *Opt. Mater. Express*, *9*(4), 1842–1863. https://doi.org/10.1364/OME.9.001842

Chen, X., Chardin, C., Makles, K., Caër, C., Chua, S., Braive, R., Robert-Philip, I., Briant, T., Cohadon, P.-F., Heidmann, A., Jacqmin, T., & Deléglise, S. (2017). High-finesse fabry-perot cavities with bidimensional si3n4 photonic-crystal slabs. *Light: Science Applications*, *6*(1), e16190–e16190. https://doi.org/10.1038/lsa.2016.190

Chen, Y.-Y. (2018). *The gander project* [Accessed: 2021-04-07]. https://steggie3.github.io/projects/gander.html

Deaton, J. D., & Grandhi, R. V. (2014). A survey of structural and multidisciplinary continuum topology optimization: Post 2000. *Structural and Multidisciplinary Optimization*, *49*(1), 1–38.

El Naqa, I., & Murphy, M. J. (2015). What is machine learning? In I. El Naqa, R. Li, & M. J. Murphy (Eds.), *Machine learning in radiation oncology: Theory and applications* (pp. 3–11). Springer International Publishing. https://doi.org/10.1007/978-3-319-18305-3_1

F450c. (n.d.). 450mm facilities and infrastructure [Accessed: 2021-03-29]. https://f450c.org/

Franssila, S. (2010). Introduction to microfabrication (2nd ed.). https://doi.org/10.1002/9781119990413

Gebisa, A. W., & Lemu, H. G. (2017). A case study on topology optimized design for additive manufacturing. *IOP Conference Series: Materials Science and Engineering*, *276*(1), 012026.

Géron, A. (2019). *Hands-on machine learning with scikit-learn, keras, and tensorflow: Concepts, tools, and techniques to build intelligent systems*. O'Reilly Media.

Giles, M. B., & Pierce, N. A. (2000). An introduction to the adjoint approach to design. *Flow, Turbulence and Combustion*, *65*(3), 393–415. https://doi.org/10.1023/A:1011430410075

Goodfellow, I. J., Pouget-Abadie, J., Mirza, M., Xu, B., Warde-Farley, D., Ozair, S., Courville, A., & Bengio, Y. (2014). Generative adversarial networks.

Harper, E. S., Coyle, E. J., Vernon, J. P., & Mills, M. S. (2020). Inverse design of broadband highly reflective metasurfaces using neural networks. *Phys. Rev. B*, *101*, 195104. https://doi.org/10.1103/PhysRevB.101.195104

Hasan, R. M. M., & Luo, X. (2018). Promising lithography techniques for next-generation logic devices. *Nanomanufacturing and Metrology*, *1*(2), 67–81. https://doi.org/10.1007/s41871-018-0016-9

Hoang, T., & Loeb, A. (2017). Electromagnetic forces on a relativistic spacecraft in the interstellar medium. *The Astrophysical Journal*, *848*(1), 31.

Hoyer, S., Sohl-Dickstein, J., & Greydanus, S. (2019). Neural reparameterization improves structural optimization.

Hughes, T., Minkov, M., Williamson, I. A. D., & Fan, S. (2018). Adjoint method and inverse design for nonlinear nanophotonic devices. *ACS Photonics*, *5*(12), 4781–4787. https://doi.org/10.1021/acsphotonics.8b01522

Hughes, T. W., Williamson, I. A. D., Minkov, M., & Fan, S. (2019). Forward-mode differentiation of maxwell's equations. *ACS Photonics*, *6*(11), 3010–3016. https://doi.org/10.1021/acsphotonics.9b01238

Ilic, O., & Atwater, H. A. (2019). Self-stabilizing photonic levitation and propulsion of nanostructured macroscopic objects. *Nature Photonics*, *13*(4), 289–295. https://doi.org/10.1038/s41566-019-0373-y

Ilic, O., Went, C. M., & Atwater, H. A. (2018). Nanophotonic heterostructures for efficient propulsion and radiative cooling of relativistic light sails. *Nano Lett.*, *18*(9), 5583–5589. https://doi.org/10.1021/acs.nanolett.8b02035

Jaxa. (n.d.). *Ikaros* [Accessed: 2021-03-29]. https://global.jaxa.jp/projects/sas/ikaros/

Jensen, J. S., & Sigmund, O. (2011). Topology optimization for nano-photonics. *Laser and Photonics Reviews*, *5*(2), 308–321. https://doi.org/10.1002/lpor.201000014

Jiang, J., & Fan, J. A. (2019). Global optimization of dielectric metasurfaces using a physics-driven neural network. *Nano Lett.*, *19*(8), 5366–5372. https://doi.org/10.1021/acs.nanolett.9b01857

Jiang, J., Sell, D., Hoyer, S., Hickey, J., Yang, J., & Fan, J. A. (2019). Free-form diffractive metagrating design based on generative adversarial networks. *ACS Nano*, *13*(8), 8872–8878. https://doi.org/10.1021/acsnano.9b02371

Jin, W., Li, W., Orenstein, M., & Fan, S. (2020). Inverse design of lightweight broadband reflector for relativistic lightsail propulsion. *ACS Photonics*, *7*(9), 2350–2355. https://doi.org/10.1021/acsphotonics.0c00768

Kao, C. Y., Osher, S., & Yablonovitch, E. (2005). Maximizing band gaps in two-dimensional photonic crystals by using level set methods. *Applied Physics B*, *81*(2), 235–244. https://doi.org/10.1007/s00340-005-1877-3

Lempitsky, V., Vedaldi, A., & Ulyanov, D. (2018). Deep image prior. *2018 IEEE/CVF Conference on Computer Vision and Pattern Recognition*, 9446–9454. https://doi.org/10.1109/CVPR.2018.00984

Li, M., Jia, G., Cheng, Z., & Shi, Z. (2021). Generative adversarial network guided topology optimization of periodic structures via subset simulation. *Composite Structures*, *260*, 113254. https://doi.org/10.1016/j.compstruct.2020.113254

Li, W., Meng, F., Chen, Y., Li, Y. f., & Huang, X. (2019). Topology optimization of photonic and phononic crystals and metamaterials: A review. *Advanced Theory and Simulations*, *2*(7), 1900017.

Liu, V., & Fan, S. (2012). S4 : A free electromagnetic solver for layered periodic structures. *Computer Physics Communications*, *183*(10), 2233–2244. https://doi.org/10.1016/j.cpc.2012.04.026

Liu, Z., Zhu, D., Rodrigues, S. P., Lee, K.-T., & Cai, W. (2018). Generative model for the inverse design of metasurfaces. *Nano Lett.*, *18*(10), 6570–6576. https://doi.org/10.1021/acs.nanolett.8b03171

Ma, W., Cheng, F., & Liu, Y. (2018). Deep-learning-enabled on-demand design of chiral metamaterials. *ACS Nano*, *12*(6), 6326–6334. https://doi.org/10.1021/acsnano.8b03569

Malkiel, I., Mrejen, M., Nagler, A., Arieli, U., Wolf, L., & Suchowski, H. (2018). Plasmonic nanostructure design and characterization via deep learning. *Light: Science Applications*, *7*(1), 60. https://doi.org/10.1038/s41377-018-0060-7

Manchester, Z., & Loeb, A. (2017). Stability of a light sail riding on a laser beam. *The Astrophysical Journal*, *837*(2), L20. https://doi.org/10.3847/2041-8213/aa619b

Martins, F. R., Pereira, E. B., & Guarnieri, R. A. (2012). Solar radiation forecast using artificial neural networks. *International Journal of Energy Science*, *2*(6), 217–217.

Men, H., Lee, K. Y. K., Freund, R. M., Peraire, J., & Johnson, S. G. (2014). Robust topology optimization of three-dimensional photonic-crystal band-gap structures. *Opt. Express*, *22*(19), 22632–22648. https://doi.org/10.1364/OE.22.022632

Mirza, M., & Osindero, S. (2014). Conditional generative adversarial nets.

Moitra, P., Slovick, B. A., Gang Yu, Z., Krishnamurthy, S., & Valentine, J. (2014). Experimental demonstration of a broadband all-dielectric metamaterial perfect reflector. *Applied Physics Letters*, *104*(17), 171102.

Molesky, S., Lin, Z., Piggott, A. Y., Jin, W., Vucković, J., & Rodriguez, A. W. (2018). Inverse design in nanophotonics. *Nature Photonics*, *12*(11), 659–670. https://doi.org/10.1038/s41566-018-0246-9

Moura, J. P., Norte, R. A., Guo, J., Schäfermeier, C., & Gröblacher, S. (2018). Centimeter-scale suspended photonic crystal mirrors. *Opt. Express*, *26*(2), 1895–1909. https://doi.org/10.1364/OE.26.001895

Myilswamy, K. V., Krishnan, A., & Povinelli, M. L. (2020). Photonic crystal lightsail with nonlinear reflectivity for increased stability. *Opt. Express*, *28*(6), 8223–8232. https://doi.org/10.1364/OE.387687

NASA. (n.d.). Voyager1 [Accessed: 2021-03-30]. https://voyager.jpl.nasa.gov/

Nikishkov, G. (2004). Introduction to the finite element method. *University of Aizu*, 1–70.

Norte, R. A., & Groblacher, S. (2021). Laser lightsail for solar system exploration.

Norte, R. A., Moura, J. P., & Gröblacher, S. (2016). Mechanical resonators for quantum optomechanics experiments at room temperature. *PRL*, *116*(14), 147202. https://doi.org/10.1103/PhysRevLett.116.147202

Odena, A., Dumoulin, V., & Olah, C. (2016). Deconvolution and checkerboard artifacts. *Distill*. https://doi.org/10.23915/distill.00003

Peurifoy, J., Shen, Y., Jing, L., Yang, Y., Cano-Renteria, F., DeLacy, B. G., Joannopoulos, J. D., Tegmark, M., & Soljačić, M. (2018). Nanophotonic particle simulation and inverse design using artificial neural networks. *Science Advances*, *4*(6). https://doi.org/10.1126/sciadv.aar4206

Pinetz, T., Ruisz, J., & Soukup, D. (2019). Actual impact of gan augmentation on cnn classification performance. *ICPRAM*, 15–23.

Salary, M. M., & Mosallaei, H. (2020). Photonic metasurfaces as relativistic light sails for doppler-broadened stable beam-riding and radiative cooling. *Laser Photonics Reviews*, *14*(8), 1900311.

Sarle, W. S. (1996). Stopped training and other remedies for overfitting. *Computing science and statistics*, 352–360.

Schamiloglu, E., Abdallah, C. T., Miller, K. A., Georgiev, D., Benford, J., Benford, G., & Singh, G. (2001). 3-d simulations of rigid microwave-propelled sails including spin. *AIP Conference Proceedings*, *552*(1), 559–564.

Sell, D., Yang, J., Doshay, S., & Fan, J. A. (2017). Periodic Dielectric Metasurfaces with High-Efficiency, Multiwavelength Functionalities. *Advanced Optical Materials*, *5*(23), 1–7. https://doi.org/10.1002/adom.201700645

Sell, D., Yang, J., Doshay, S., Yang, R., & Fan, J. A. (2017). Large-Angle, Multifunctional Metagratings Based on Freeform Multimode Geometries. *Nano Letters*, *17*(6), 3752–3757. https://doi.org/10.1021/acs.nanolett.7b01082

Sigmund, O., & Petersson, J. (1998). Numerical instabilities in topology optimization: A survey on procedures dealing with checkerboards, mesh-dependencies and local minima. *Structural optimization*, *16*(1), 68–75.

Su, L., Vercruysse, D., Skarda, J., Sapra, N. V., Petykiewicz, J. A., & Vučković, J. (2020). Nanophotonic inverse design with spins: Software architecture and practical considerations. *Applied Physics Reviews*, *7*(1), 011407.

Svanberg, K. (1987). The method of moving asymptotes–a new method for structural optimization. *Int. J. Numer. Meth. Engng.*, *24*(2), 359–373. https://doi.org/10.1002/nme.1620240207

Szegedy, C., Ioffe, S., Vanhoucke, V., & Alemi, A. (2017). Inception-v4, inception-resnet and the impact of residual connections on learning. *Proceedings of the AAAI Conference on Artificial Intelligence*, *31*(1). https://ojs.aaai.org/index.php/AAAI/article/view/11231

van Dijk, N. P., Maute, K., Langelaar, M., & Van Keulen, F. (2013). Level-set methods for structural topology optimization: A review. *Structural and Multidisciplinary Optimization*, *48*(3), 437–472.

Wentzel-Long, M., & Landis, G. A. (2020). Power generation from interplanetary and interstellar plasma and magnetic fields. *AIAA Propulsion and Energy 2020 Forum*, 3537.

Zhang, Y., & Wallace, B. (2016). A sensitivity analysis of (and practitioners' guide to) convolutional neural networks for sentence classification.

Zhang, Z., Wang, R., & Xue, D. (2018). Microfabrication by laser lithography combined with ion etching. In J. Yan (Ed.), *Micro and nano fabrication technology* (pp. 1–28). Springer Singapore. https://doi.org/10.1007/978-981-10-6588-0_18-1

3

A NEURAL NETWORK BASED APPROACH FOR LIGHTSAIL DESIGN

This chapter is written as a scientific paper. First, the paper discusses implementing a novel ML-based TO method for lightsail design. The ML-based TO is then benchmarked against a more traditional TO. Lastly, new designs are generated with the implemented novel ML-based TO by considering additional operational conditions.

Lightsail design with neural optimization of topology

Lucas Norder
(Dated: February 10, 2022)

Conventional Topology Optimization (TO) enables the inverse design of nanophotonic structures by specifying the objective and constraints without a predefined topological concept. Yet, extreme scenarios such as the design of a lightsail pose challenges that require new solutions. Here, a convolutional neural network (CNN) based TO methodology is extended to optimize a two-dimensional photonic crystal used to design a lightsail that aims to reach the nearest star (Alpha Centauri) within 20 years by achieving 20% of the speed of light. The CNN-TO performance is compared to a more conventional method of moving asymptotes (MMA) based TO by optimizing a photonic crystal unit-cell for the 2016 Starshot Initiative parameters. The CNN-TO requires up to 40% fewer iterations than MMA-TO to reach better performance under different operational conditions. The generated design turned out to be easy to fabricate, allowing them to be produced with optical lithography. Additionally, a study regarding the design challenges of the lightsail has been performed, which resulted in an optimization considering the functionallity of the sail. Additionally, the study showed the sensitivity of the resulting design to varying objectives and materials. Therefore, underlining the necessity of considering multiple operating conditions (e.g. laser alignment and cooling) within the design process.

I. INTRODUCTION

At the moment, the man-made object furthest from earth is the Voyager 1 [1]. Although this spacecraft has seen our solar system and beyond, it only travelled 0.5% of the distance to the nearest solar system after 47 years of service. New spacecrafts are required to explore these unknown worlds. Breakthrough Initiatives started the Starshot Initiative in 2016 to stimulate the development of lightsails [2]. This spacecraft aims to reach Alpha Centauri (i.e. the nearest star to earth) within 20 years by reaching speeds up to 20% of the speed of light.

This technology, presented in Fig. 1, is based on generating an optical force on a reflective lightweight thin-film material by projecting a high power Earth-based laser on it. As proposed in the Starshot initiative, the lightsail should be approximately 10 m^2 and the laser power 10-100 GW/m^2 to generate enough radiation pressure. Furthermore, extreme low-mass requirements have been proposed, limiting the weight of the sail and the satellite chip connected to it to approximately 1 g. The laser is also required to operate on wavelengths in the near-infrared spectrum from 1 - 1.5 μm.

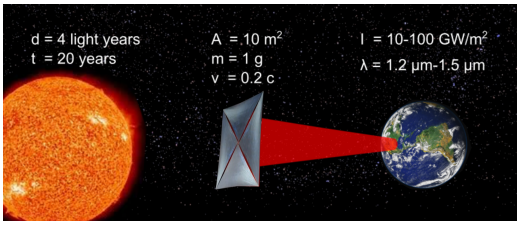

FIG. 1. High power earth-based laser propelling lightweight sail to 20% of the light speed, to reach Alpha Centauri in 20 years [2].

Traditional metallic reflectors cannot be used due to their high optical absorption. Semiconductors have the potential to meet the operating requirements as they have a high refractive index and low optical absorption. To meet the mass and reflectivity requirements a thickness estimation of 100 atomic layers for the sail is deemed necessary [3]. Such stringent requirements have motivated research on one- and two-dimensional photonic crystals (PhC) as broadband reflectors [3]. A PhC is a structure with sub-wavelength sized features that interact with light. One-dimensional periodic PhCs are stacked materials with different dielectric constants, while two-dimensional PhCs are planar structures with periodic designs (e.g. holes or pillars). Given the additional design freedom, two-dimensional PhCs are expected to provide higher reflectivity for a critical area density [4, 5] .

Although two-dimensional PhC's have proven to be effective reflectors even with simple designs [6, 7], the few contributions targeting lightsail design have not considered operational and manufacturability conditions sufficiently [3, 8, 9]. Moreover, the traditional optimization of photonic structures is highly iterative and leverages domain knowledge from experienced researchers [10]. However, this trial-and-error process is unlikely to be successful in finding high-performance designs because there are too many possibilities to be explored within the high dimensional design space.

Inverse design methods like topology optimization (TO) have shown promising results for the design of photonic devices like meta-devises and photonic crystals [11–14]. More traditional TO-algorithms based on level-set, SIMP and even genetic optimization algorithms are used for these applications [11, 12] although it is unlikely that they reached a global optimum. Although Photonics optimization is usually non-linear, non-convex and high dimensional, inverse design methods have resulted in non-trivial high-performance designs [13, 14].

Recently, however, TO has been enhanced by machine learning via the reparameterization trick proposed by Hoyer et al. [15]. This strategy is different from the majority of machine learning contributions that improve design methods because those involve training with previous designs or involving Variational Autoencoders and Generative Adversarial Neural Networks [16–18] that require large training databases and that have difficulties with out-of-distribution predictions. In contrast, the reparameterization trick introduces a neural network before the physics solver (e.g. finite element analyses) and uses common machine learning optimizers to find the weights and biases of the neural network that minimize the objective function calculated by the physics solver. Albeit counter-intuitive, this strategy was shown to outperform conventional TO algorithms that optimize the objective function directly acting on the inputs of the physics solver.

An important design target for lightsails is the minimization of the acceleration distance (D), i.e. the distance required to reach the final velocity of the lightsail. This quantity of interest enforces a trade-off between weight and reflectivity [19]. The acceleration distance is presented in Eq. (1).

$$D = \frac{c^3}{2I}(\rho_l + \rho_s) \int_0^{\beta_f} \frac{h(\beta)}{R[\lambda(\beta)]}\, d\beta \tag{1}$$

In this equation, D is the acceleration distance, I is the intensity of the propulsion laser, ρ_l and ρ_s are the area densities of the lightsail and the satellite respectively, λ is the wavelength of the propulsion laser, R is the reflection as a function of λ, and $h(\beta) = \beta/(1-\beta)^2\sqrt{1-\beta^2}$, where β is the velocity fraction with respect to the speed of light $\beta = v/c$. Due to the Doppler red-shift of the laser, the wavelength of the laser can be written as a function of the relative speed, $\lambda(\beta) = \lambda_0\sqrt{(1+\beta)/(1-\beta)}$. When following standard Starshot parameters, the bandwidth at which the sail should operate is from 1.2 μm to 1.44 μm. ρ_l and R are the geometry dependent parameters.

This work aims at minimizing D by adapting the neural optimization of topology strategy proposed by Hoyer et al. [15] to the lightsail design problem. This requires a different physics analysis method and a different neural network architecture than what was proposed originally for structural optimization problems. The work of Jin et al. [20] acts as a baseline for this investigation, as they implemented a conventional TO approach to design a two-dimensional PhC unit-cell for a lightsail following the Starshot parameters. The physics analysis from this method is implemented in the machine learning TO and the results are compared.

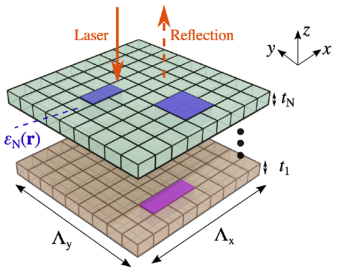

FIG. 2. Schematic of lightsail optimization [20]. The lightsail can be optimized for stacked layers of different material of thickness t. The unit cell with the periodicity of Λ is optimized. The discretized voxels of material have the dielectric constant $\epsilon_N(r)$ assigned to them.

II. TOPOLOGY OPTIMIZATION IN LIGHTSAIL DESIGN

Recently, Jin et al. [20] designed two-dimensional PhC's for lightsails using free-form TO. The authors claimed to have up to 50% better performance than previous designs by using the conventional Method of Moving Asymptotes (MMA-TO). Therefore, the two-dimensional design space is discretized into a grid of $N \times N$ pixels and the material properties of these pixels can be continuously varied between vacuum and the required material. These $N \times N$ density input parameters are then optimized using a sinh intermediate density penalization [21]. Furthermore, the unit cell's period Λ (i.e. the lattice vector) is used as an optimization parameter, while the layer thickness t is seen as an independent simulation parameter. A schematic overview of the optimization and the parameters is presented in Fig. 2. The optimization has a variable mesh size as the period Λ is an optimization variable and can be determined by dividing the period by the grid size N.

As mentioned, the gradient-based optimizer Method of Moving Asymptotes (MMA) is used to manage the many design variables [22]. The optimization algorithm uses adjoint variables to calculate the gradients of the figure of merit (FOM) with respect to the design variables. The gradients are then used to change the design variables for the following iteration. These adjoint variables are obtained from the physics simulator, which is extended with the automated differentiation software Autograd [23]. For the physics simulation, rigorous coupled-wave analysis (RCWA) is used because this semi-analytical method is computationally efficient in solving scattering problems for periodic structures with layers that are invariant in the direction normal to the periodicity [24]. The RCWA solves the time-harmonic Maxwell's equations, presented in Eq. (2), in Fourier domain. In Eq. (2), $\mathbf{E}$ and $\mathbf{H}$ are the electric and magnetic field respectively, μ_0 is the magnetic permeability, ϵ_0 is the relative

permittivity of vacuum, ϵ is the relative permittivity of the medium where the electromagnetic wave with frequency ω is passing through [25].

$$\nabla \times \mathbf{E} = -i\omega\mu_0\mathbf{H}, \ \nabla \times \mathbf{H} = i\omega\epsilon_0\epsilon\mathbf{E} \tag{2}$$

In the RCWA, the electric field for each layer is obtained by solving their eigenvalue problem. The different layers are then combined in a scattering matrix which can be used to calculate the reflection, transmission and deflection by satisfying field continuity [25, 26]. The reflectivity is then used to calculate the acceleration distance D as the FOM.

The proposed MMA-TO does not behave well when optimizing structures made from a high refractive index material. These materials result in many narrowband resonance peaks when used in the optimization of a PhC. A relaxation factor (Q) that adds a non-physical absorption loss to the material is introduced to cope with this [20]. The non-physical absorption broadens the high resonance response and is analogous to damping in a mechanical system. This facilitates convergence of the simulation when using a small Q (e.g. $Q \approx 50$) but if $Q \to \infty$ it becomes a true scattering problem. Additional details are presented in Appendix A.1.

In this work, a new machine learning enhanced TO approach proposed by Hoyer et al. [15] is explored in an attempt to reach better solutions and alleviate some of the numerical issues encountered in conventional TO. Hoyer et al. noted that CNNs contain "deep image priors" [27], i.e. they can perform tasks in image processing even before being trained. The authors showed that this strategy outperforms conventional TO algorithms for a wide range of mechanical structural optimization problems by generating simpler structures that have lower compliance within fewer iterations. In principle these performance gains should be observed for the lightsail optimization problem too, despite the physics solver being based on RCWA simulations (photonics) instead of structural finite element analyses (solid mechanics).

The working principle of the algorithm is presented in Fig. 3. The algorithm consists of 4 parts: the CNN, the post-processing, functional analysis and figure of merit (FOM) [28]. The optimization consists of a forward and a backward step. In the forward step, a randomized vector β is put into the CNN, which outputs an image of the optimized structure. This image is then filtered, after which the performance parameters obtained in the functional analysis can be used to determine the FOM. In the backward step, the gradients with respect to the FOM are calculated for all the trainable variables of the CNN and the elements of β so that the L-BFGS [29] optimizer can be used to update them at each new iteration. This procedure is repeated until the FOM reaches a preset relative tolerance or a maximum number of iterations is reached.

The original CNN-TO is modified to perform the same optimization task as the MMA-TO by changing the

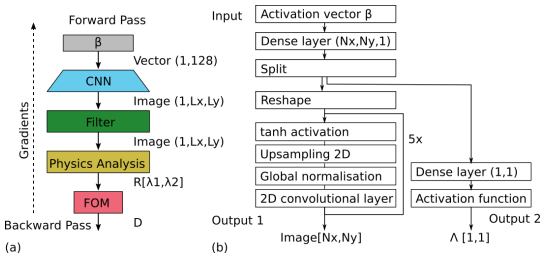

FIG. 3. (a) The ML based TO proposed by Hoyer consists of a input vector β, CNN, post processing step, function analysis and the calculation of the FOM. Automatic differentiation is used to calculate the gradients with respect to the FOM for the tunable variables.(b) The modified NN. One element is added to the first dense layer, which is split into a separate branch holding one dense layer consisting of one node.

physics analysis from a finite element method (FEM) to RCWA and modifying the CNN to add the period of the PhC (Λ) as an optimization parameter. Appendix B.1 elaborates on the modifications of the original CNN.

The modified CNN starts with β as the input to the first dense layer. From this point, the CNN is split into two branches. The first branch, which generates the design, is a generative CNN based on a U-net architecture [27]. This branch is split into 32 image channels on which the following operations are repeated five times: tanh activation function, 2D upsampling, global normalization, and a 2D convolutional layer. The 2D upsampling is only performed two of the five times. The second branch, which outputs Λ, is split into one neuron, followed by an activation function.

A modified hyperbolic tangent is chosen as the activation function because bounds can be set on the extra optimization variable and the initial solution of this variable can be influenced, as detailed in Appendix B.2.

For both TO algorithms, the objective is to minimize acceleration distance D for a crystalline silicon (c-Si) lightsail following the 2016 Starshot parameters. The optimization formulation is presented in Eq. (3) where x_{ij} is the density field and Λ is the unit cell's period, both of which need to be found such that D is minimized. The density of c-Si is considered to be 2329 kg/m^3 and its refractive index is 11 [3]. The intensity I of the laser beam is 10 GW/m^2 with a wavelength λ of 1.2 μm. The laser is assumed to be a linear polarised plane wave, and the sail area is 10 m^2. The initial solution of the material distribution x_{ij} is set to be random, and the initial solution of the period Λ is set to be the laser wavelength λ. The maximum period is set to be three times the laser wavelength. The design space is divided into a 100 $\times$ 100 pixel grid. As the base line for this work the recreated optimization from Jin et al. [20] is used. Additional information regarding the baseline optimization is presented in Appendix A.4.

$$\begin{aligned} \min_{x_{ij},\Lambda} \quad & D(R(x_{ij},\Lambda)) \\ \text{subject to} \quad & \nabla\times\mathbf{E} = -i\omega\mu_0\mathbf{H},\ \nabla\times\mathbf{H} = i\omega\epsilon_0\epsilon\mathbf{E}\ , \\ & 0 \le x_{ij} \le 1\ \forall(i,j), \\ & 0.1\mu m \le \Lambda \le 3.6\mu m. \end{aligned} \tag{3}$$

III. COMPARISON OF THE TO ALGORITHMS

At first, a mesh convergence study was performed to determine the required grid size. Interestingly, this investigation revealed that the CNN-TO methodology has less mesh dependency than MMA-TO. As discussed in the Appendix A.3, the subsequent results are obtained for a grid of 100 × 100 pixel.

The MMA-TO solutions obtained by Jin et al. (2019) have been replicated by optimizing PhC's with fixed thicknesses from 10 nm to 500 nm. Ten different randomization seeds have been used for both the MMA-TO and the CNN-TO in order to ensure that the results are not particular for a given (random) initial conditions. The stopping criterion for the optimization was set to a relative tolerance of 10^{-6} for the FOM. Furthermore, the structure is optimized with $Q = 50$ followed by $Q \to \infty$ (i.e. a true scattering problem), for a maximum number of iterations of 1000 and 100 respectively. For both methods, the original hyperparameters were used.

The mean number of iterations from these optimizations are presented in FIG. 4. What stands out from this figure is that the CNN-TO uses up to 40% fewer iterations compared to the MMA-TO. FIG. 5a provides an overview of the obtained D from the different optimizations. The figure shows that the CNN-TO and the MMA-TO obtain the same results for the best solution and similar results for the mean obtained D. Representative best designs are presented in FIG. 5b,c. Notably, the best designs for $t \le 30$ nm and $t \ge 50$ nm are sheets and strings respectively. A selection of the resulting designs and their equivalent loss history is presented in appendix C.1.

Interestingly, the MMA-TO and CNN-TO execute one iteration in approximately 16 sec. This is unexpected as the CNN-TO has more than 300×10^3 optimization variables and the MMA-TO approximately 10×10^3. Therefore, it is expected that the method with more optimization variables would take more time per iteration, as it requires more arithmetic operations. FIG. 6 shows the relative and absolute time spent on the gradient, FOM and other calculations by both TO algorithms. The graph shows that the MMA-TO spends relative and absolute more time computing the gradients than the CNN-TO. Since the libraries Tensorflow [30] for the CNN-TO and nlopt [31] for the MMA-TO both use Autograd to calculate the gradients, it is likely that the implementation of the nlopt libary is less efficient and resulting in long optimization times. This results in a distorted comparison as the iteration time is dependent on the method and its implementation.

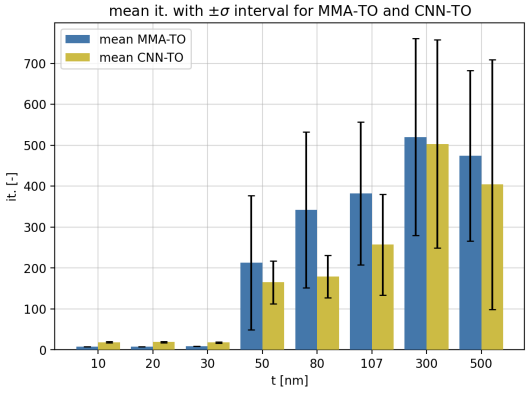

FIG. 4. The mean iterations used for the MMA-TO and the CNN-TO for 10 different randomization seeds, σ is the standard deviation.

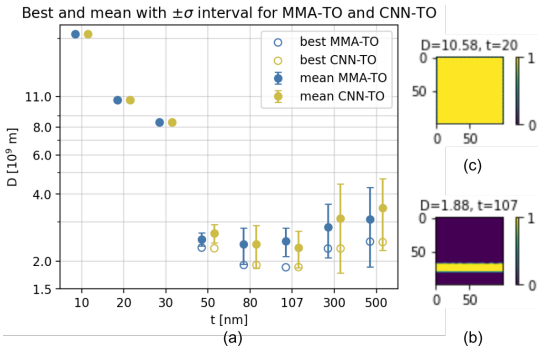

FIG. 5. (a) Best and mean designs for MMA-TO and CNN-TO for 10 different randomization seeds, (b) representative sheet designs for $t \ge 50$ nm, (c) representative string design for $t \le 30$ nm. For each design yellow indicates material and blue vacuum, σ is the standard deviation.

IV. PRACTICAL DESIGN CONSIDERATIONS

A significant problem with the designs presented in FIG. 5 is that they are not practical to fabricate. Submicron meter thin tethers spanning cm or m wide gaps will inevitably fail. In the previous section, the lightsail was optimized for a linear polarised plane wave normally incident on the sail, resulting in the string design. These strings in the PhC are observed to align with the polarisation direction when axially rotated. Therefore, changing the operating conditions by finding a more suitable

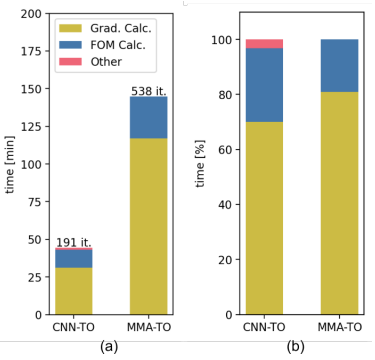

FIG. 6. Code profiling done for one seed, optimizing a PhC with t is 107 nm using the MMA-TO and the CNN-TO. The absolute (a) and relative (b) time the needed of the gradients, FOM and other computations.

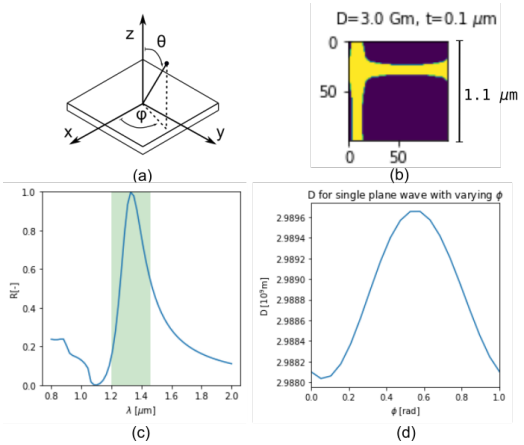

FIG. 7. Best optimized PhC from 10 different randomization seeds for $\phi = 0°$ and $\phi = 90°$ considering thickness t, material density and Λ as optimization parameters. The resulting designs have D=3.0 Gm, Λ=1.06 μm and t=0.10 μm. (a) definition of axis, (b) best design using the MMA-TO and CNN-TO where yellow indicates is material and blue vacuum, (c) reflectivity of the PhC for $\phi = 0°$ and for different wavelengths, where the green area shows the operating bandwidth of the sail, (d) the acceleration distance D for the design shown in (b) illuminated by a single polarized plane wave for varying angle (ϕ).

FOM is expected to lead to a different design that does not have these strings.

In practice, aligning the laser with the lightsail in space would be a severe challenge. There is a high probability that the sail is rotated around its normal (ϕ), tilted with respect to the incoming laser (θ) or even constantly rotating (FIG. 7a). Appendix D.1 shows that the string design presented in Fig. 5b will lose its performance when rotated by ϕ as the sail is optimized for only one orientation of the laser. Therefore, the lightsail requires optimization for multiple polarization angles.

This alignment issue can be incorporated in the FOM by taking the mean D for multiple angles of ϕ. For the first optimization, ϕ is chosen to be 0° and 90°, because any other polarisation angle is a projection of these orientations. Additionally, besides the material distribution and Λ, the thickness (t) of the PhC is added as an optimization variable to generalize the TO further. The bounds for t were set to 0.01 μm - 1 μm and initialized at 0.1 μm. The new optimization formulation is presented in Appendix D.1. The optimization was performed with the MMA-TO and the CNN-TO for ten different randomization seeds using the optimization parameters described above. FIG. 7 shows that the best result from this optimization is a two-dimensional PhC consisting of square holes, which is a similar result to the one reported in the supporting documentation of Jin et al. (2020)[20]. The acceleration distance D for this PhC, optimized for two orthogonal polarisation angles and illuminated by a single plane wave for varying ϕ, as well as the reflectivity of the PhC for $\phi = 0°$ can be seen in Fig. 7c and 7d, respectively. This shows that the D varies less than 1% for the different polarisation directions, indicating that optimizing for two orthogonal polarisation directions can reduce the lightsail performance's dependency with the incident laser's polarisation direction. Both TO methods result in the same best design. However, TABLE I shows

TABLE I. Results from the TO of a PhC for two orthogonal polarization direction. $\overset{*}{D}$ is the best result, $\bar{D}$ is the mean result obtained and $\bar{it}$ is the mean number of optimization iterations.

Method	$\overset{*}{D}$ $[10^9 m]$	$\bar{D}[10^9 m]$	$\bar{it}[-]$
MMA-TO	3.0	4.4±1.6	1328±760
CNN-TO	3.0	3.8±1.3	1047±645

that the CNN-TO uses fewer iterations, resulting in a lower mean D. Remarkably, the difference between the CNN-TO and the MMA-TO is more pronounced than what was obtained in FIG. 4 and 5.

In addition, this optimization was also performed considering different grid sizes. As discussed previously, the CNN-TO is less mesh dependent than MMA-TO for problems solved with a fine mesh. The results shown in FIG. 8 reinforce this finding, as the best and the mean acceleration distance D for five different randomization seeds clearly show that for high-dimensional problems the MMA-TO solution requires long optimization times and reaches a significantly worst D (a rough estimate is to avoid $> 10^4 - 10^5$ parameters for MMA-TO in this context) [31, 32]. The two optimizations performed by the MMA-TO for a grid with $N = 200$ and $N = 300$ did not converge to a single design. It is likely that the large

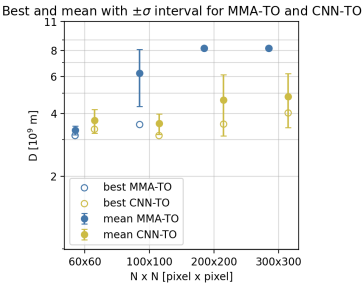

FIG. 8. Obtained best and mean acceleration distance D for optimization performed with CNN-TO and MMA-TO for varying design grid size ($N \times N$), σ is the standard deviation.

number of variables in combination with the high dimensionality of the PhC problem resulted in a stagnating optimization.

Notwithstanding the above stated, it should be noted that both TO methods have been considered with their original hyperparameters. Therefore, the conclusion that MMA-TO performs worse than CNN-TO only remains valid if the dependency of the hyperparameters of both algorithms is investigated, as they can have a major impact on for specific tasks.

In essence, both TO methods have their strengths and weaknesses. MMA-TO is a well-known method that is properly documented and can be easily implemented. The CNN-TO seems to provide a performance improvement but it is less trivial to implement and to use because there are many hyperparameters. For example, this investigation did not consider significant changes in the neural network architecture. Small changes of the architecture or the optimization parameters could lead to significant impact in performance (although the results obtained for the proposed architecture showed to be robust). An example for this is provided in appendix B.3. Additionally, it is not transparent how changes in the optimization parameters will affect the outcome, making modifying the TO a trial and error process. Nevertheless, the CNN-TO has generated good designs even for large design spaces, without changing any of the original CNN's hyperparameters. Therefore, for the final optimization investigations of this work only the CNN-TO is used, as it shows faster convergence for more complex problems.

Additional to using the mean acceleration distance for two orthogonal polarisation directions, multiple angles of ϕ were considered (e.g. ϕ as 0°, 45° and 90°). Furthermore, the misalignment of the lightsail is considered by taking the mean acceleration distance from θ as 0°, 5° and 10° and considering $\phi = 0°$ and $\phi = 90°$. However, the best designs obtained using this extended FOM resulted in the same designs as shown in Fig. 7b. This approach is described in more detail in appendix D.1.

V. HEATING OF THE SAIL

Another practical issue to overcome in the design of lightsails is the fact that they heat as a consequence of the laser incidence [3, 8, 33]. Eq. 4 shows the expression to calculate the maximum temperature (T_{max}) of the sail during acceleration [33]. In this equation P_{laser} is the power of the laser, α_{sail} the assumed normalized sail absorption, and A_{sail} the area of the sail, $c_1 = 2\pi hc^2$, $c_2 = hc/k_b$, k_b is the Boltzmann constant, h is Planck's constant, c is the speed of light, ϵ_{sail} is the emissivity of the sail.

$$P_{laser}\alpha_{sail} = 2A_{sail}\int_{\lambda_0}^{\lambda_1} \frac{c_1}{\lambda^5} \frac{\epsilon_{sail}(\lambda)}{e^{\frac{c_2}{\lambda T_{max}}} - 1}\, d\lambda \tag{4}$$

To prevent the sail from melting, a material with low optical absorption (α) and high emissivity (ϵ) in the mid-infrared spectrum ($2.5\mu m - 20\mu m$) is required [8]. The A_{sail} is the design-dependent parameter inversely related to the T_{max}, so the heating problem can be incorporated within the TO by maximizing A_{sail} while also minimizing D. Therefore, these two objectives create a trade-off between the area and the thickness of the PhC to reduce the mass of the sail. The A_{sail} is introduced in the TO as an area constraint, which is satisfied by using a constrained sigmoid transformation as presented in Eq. 5 [15].

$$\begin{aligned} x_{ij} = 1/(1 + exp[\hat{x_{ij}} - b(\hat{x}, A_0)]), \\ \text{such that: } A(x) = A_0 \end{aligned} \tag{5}$$

In this equation x is the constraint density field, $\hat{x}$ is the unconstrained density field, A_0 is the constraint area fraction and $b(\hat{x}, A_0)$ is solved through a binary search on the area constraint.

The optimization was performed considering a parameter sweep for A_0 from 40%-60%. The best PhC's and corresponding mean acceleration distance D are shown in FIG. 9a, where $\phi = 0°$ and $\phi = 90°$ and $A_0 = 45\%$. This design is a two-dimensional PhC following a Cairo pentagonal lattice [34]. Notably, no designs following this type of lattices have been reported up to now in the lightsails literature. The correct T_{max} for the sail cannot be determined as there is a lack of precision measurements for ϵ and α for representative operating conditions for c-Si [33, 35, 36]. This design and its resulting properties are discussed in more detail in appendix D.2.

Optimization with other materials

The previous optimizations were performed for a c-Si PhC, following the baseline study of Jin et al. (2019). However, there are other materials that can be good candidates for this problem, such as MoS_2 and SiN [3, 9, 20, 37]. Among these materials, SiN has one of the

highest potentials for the lightsail application because it has the lowest optical absorption, has been successfully adopted for manufacturing different photonic devices, has low density and will not wrinkle due to the internal stresses generated in the production [5, 38, 39]. Given these favourable properties, the optimization for two polarisation directions is also performed for this material. For reference, SiN has higher density than c-Si (3100 kg/m^3) and lower dielectric constant (4) [5, 38].

FIG. 9 shows that the best design using SiN follows the same shape as with c-Si. Furthermore, the Area constraint did also result in a different design. However, the design optimized with the area constraint has the lowest acceleration distance. This shows that the resulting designs are dependent on the initial solution and the constraints. The best design without and with the area constraint has an area percentage of 36% and 60% respectively, and their T_{max} with respect to the laser power is presented in FIG. 9c. This graph shows that there can be a 9%-14% reduction in T_{max} when applying the area constraint. Incorporating the area constraint in the TO will result in a higher D. However, depending on the values for α and ϵ, it can be a factor for staying under the maximum operating temperature. The melting temperature of SiN is indicated with a red line as the maximum sail temperature in FIG. 9c. In practice, this is not correct as the material will lose its mechanical properties at lower temperatures.

In summary, applying the area constraint showed that introducing multiple operating conditions can drastically change the lightsail design and that it can be used to generate thicker features. Additionally, the designs showed that the optimization was more sensitive to initial solutions when optimizing for SiN than c-Si. The optimizer might get stuck in a local optimum due to the lower dielectric constant for SiN, leading to lower reflectivity variation for different designs. This highlights that the material used in the optimization affects the optimization process for this problem. The optimization for the SiN lightsail is discussed in more detail in appendix D.3.

The most striking result that emerges from the designs shown in FIG. 9 is their feature size. The idea of the Starshot initiative is to increase the chance of reaching Alpha Centauri by sending a fleet of lightsails into space. Therefore, having a production method to pattern m^2 sized sails with high throughput and low cost is crucial to the mission's success. At the moment, the cheapest and fastest nanofabrication method is optical lithography. Defining the minimum feature size (MFS) for optical lithography is hard because it depends on many parameters, and different production techniques can be applied to achieve a specific shape. It is reported that standard optical lithography has a MFS around 500 nm [40]. Knowingly, this method could be easily applied when the design features are around 1 μm, the designs presented in FIG. 9 have dimensions that allow fabrication by optical lithography. However, this does not consider the actual shape of the design, having large and dull features

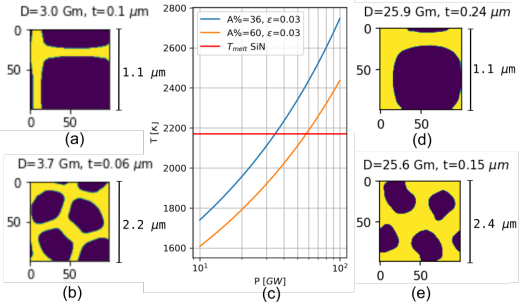

FIG. 9. Optimization with area constraint. For each design, yellow indicates material and blue vacuum. Best design without (a) and with area constraint(b) for c-Si with A_0 is 45%. (c) T_{max} for ϵ is 0.03 [36], constant α of 10^{-6} and A_0 is 60% for SiN. (d) best design for SiN with no area constraint, (e) best design with area constraint for SiN with A_0 is 60%.

in the design would reduce the stress concentrations in the structure, thus making it more resilient to the acceleration forces. Including production constraints within the optimization is essential for further development of the lightsail.

VI. CONCLUSION

In this work a CNN-TO and MMA-TO is applied to the lightsail problem, following the 2016 Starshot parameters. The CNN-TO uses up to 40% fewer iterations than the MMA-TO. Although the CNN-TO is non-trivial to implement, it is shown that for large and high-dimensional design problems this method results in high-performance and non intuitive lightsail designs, without needing to change the CNN architecture and its hyperparameters for different problems. However, the MMA-TO might be marginally better suited than the CNN-TO for smaller design spaces ($< 10^4$ design variables).

Optimizing the lightsail for multiple polarisation angles includes the misalignment of the sail with the laser in the objective and results in easy to produce two-dimensional PhC. Furthermore, the study has shown that the material of the lightsail can have a major impact on the optimization and the final design of the lightsail. Additionally, it is shown that considering operational conditions can significantly change the final design of the lightsail, and implementing additional constraints (e.g. production and mechanical constraints) can be essential for practical designs.

[1] NASA, Voyager1, Accessed: 2021-03-30.

[2] Breakthrough Initiatives, Starshot, accessed: 2021-03-29.

[3] H. A. Atwater, A. R. Davoyan, O. Ilic, D. Jariwala, M. C. Sherrott, C. M. Went, W. S. Whitney, and J. Wong, Materials challenges for the starshot lightsail, Nature Materials **17**, 861 (2018).

[4] R. A. Norte, J. P. Moura, and S. Gröblacher, Mechanical resonators for quantum optomechanics experiments at room temperature, PRL **116**, 147202 (2016).

[5] J. P. Moura, R. A. Norte, J. Guo, C. Schäfermeier, and S. Gröblacher, Centimeter-scale suspended photonic crystal mirrors, Opt. Express **26**, 1895 (2018).

[6] P. Moitra, B. A. Slovick, Z. Gang Yu, S. Krishnamurthy, and J. Valentine, Experimental demonstration of a broadband all-dielectric metamaterial perfect reflector, Applied Physics Letters **104**, 171102 (2014).

[7] S. Bernard, C. Reinhardt, V. Dumont, Y.-A. Peter, and J. C. Sankey, Etch-tuning and design of silicon nitride photonic crystal reflectors (2016), arXiv:1609.00858 [physics.optics].

[8] O. Ilic, C. M. Went, and H. A. Atwater, Nanophotonic heterostructures for efficient propulsion and radiative cooling of relativistic light sails, Nano Lett. **18**, 5583 (2018).

[9] K. V. Myilswamy, A. Krishnan, and M. L. Povinelli, Photonic crystal lightsail with nonlinear reflectivity for increased stability, Opt. Express **28**, 8223 (2020).

[10] Z. Liu, D. Zhu, S. P. Rodrigues, K.-T. Lee, and W. Cai, Generative model for the inverse design of metasurfaces, Nano Lett. **18**, 6570 (2018).

[11] J. S. Jensen and O. Sigmund, Topology optimization for nano-photonics, Laser and Photonics Reviews **5**, 308 (2011).

[12] W. Li, F. Meng, Y. Chen, Y. f. Li, and X. Huang, Topology optimization of photonic and phononic crystals and metamaterials: A review, Advanced Theory and Simulations **2**, 1900017 (2019).

[13] S. Molesky, Z. Lin, A. Y. Piggott, W. Jin, J. Vucković, and A. W. Rodriguez, Inverse design in nanophotonics, Nature Photonics **12**, 659 (2018).

[14] S. D. Campbell, D. Sell, R. P. Jenkins, E. B. Whiting, J. A. Fan, and D. H. Werner, Review of numerical optimization techniques for meta-device, Opt. Mater. Express **9**, 1842 (2019).

[15] S. Hoyer, J. Sohl-Dickstein, and S. Greydanus, Neural reparameterization improves structural optimization (2019), arXiv:1909.04240 [cs.LG].

[16] W. Ma, F. Cheng, and Y. Liu, Deep-learning-enabled on-demand design of chiral metamaterials, ACS Nano **12**, 6326 (2018).

[17] J. Jiang, D. Sell, S. Hoyer, J. Hickey, J. Yang, and J. A. Fan, Free-form diffractive metagrating design based on generative adversarial networks, ACS Nano **13**, 8872 (2019).

[18] J. Peurifoy, Y. Shen, L. Jing, Y. Yang, F. Cano-Renteria, B. G. DeLacy, J. D. Joannopoulos, M. Tegmark, and M. Soljačić, Nanophotonic particle simulation and inverse design using artificial neural networks, Science Advances **4**, 10.1126/sciadv.aar4206 (2018), https://advances.sciencemag.org/content/4/6/eaar4206.full.pdf.

[19] A. Macchi, S. Veghini, and F. Pegoraro, "light sail" acceleration reexamined, Phys. Rev. Lett. **103**, 085003 (2009).

[20] W. Jin, W. Li, M. Orenstein, and S. Fan, Inverse design of lightweight broadband reflector for relativistic lightsail propulsion, ACS Photonics **7**, 2350 (2020), https://doi.org/10.1021/acsphotonics.0c00768.

[21] J. D. Deaton and R. V. Grandhi, A survey of structural and multidisciplinary continuum topology optimization: post 2000, Structural and Multidisciplinary Optimization **49**, 1 (2014).

[22] K. Svanberg, A class of globally convergent optimization methods based on conservative convex separable approximations, SIAM journal on optimization **12**, 555 (2002).

[23] D. Maclaurin, D. Duvenaud, and R. P. Adams, Autograd: Effortless gradients in numpy, in *ICML 2015 AutoML Workshop*, Vol. 238 (2015) p. 5.

[24] W. Jin, grcwa: rigorous coupled wave analysis supporting automatic differentation with autograd; (2020).

[25] V. Liu and S. Fan, S4 : A free electromagnetic solver for layered periodic structures, Computer Physics Communications **183**, 2233 (2012).

[26] S. Yu, C. Wang, C. Sun, and W. Chen, Topology optimization for highly-efficient light-trapping structure in solar cell, in *10th world congress on structural and multidisciplinary optimization, Orlando* (2013).

[27] V. Lempitsky, A. Vedaldi, and D. Ulyanov, Deep image prior, in *2018 IEEE/CVF Conference on Computer Vision and Pattern Recognition* (2018) pp. 9446–9454.

[28] S. G. Stephan Hoyer, Jascha Sohl-Dickstein, Neural reparameterization improves structural optimization (2019).

[29] J. Nocedal, Updating quasi-newton matrices with limited storage, Mathematics of computation **35**, 773 (1980).

[30] M. Abadi, A. Agarwal, P. Barham, E. Brevdo, Z. Chen, C. Citro, G. S. Corrado, A. Davis, J. Dean, M. Devin, S. Ghemawat, I. Goodfellow, A. Harp, G. Irving, M. Isard, Y. Jia, R. Jozefowicz, L. Kaiser, M. Kudlur, J. Levenberg, D. Mané, R. Monga, S. Moore, D. Murray, C. Olah, M. Schuster, J. Shlens, B. Steiner, I. Sutskever, K. Talwar, P. Tucker, V. Vanhoucke, V. Vasudevan, F. Viégas, O. Vinyals, P. Warden, M. Wattenberg, M. Wicke, Y. Yu, and X. Zheng, TensorFlow: Large-scale machine learning on heterogeneous systems (2015), software available from tensorflow.org.

[31] S. G. Johnson, Nlopt algorithms, Accessed: 2022-01-13.

[32] K. Svanberg, A class of globally convergent optimization methods based on conservative convex separable approximations, SIAM Journal on Optimization , 555.

[33] J. Brewer, M. F. Campbell, P. Kumar, S. Kulkarni, D. Jariwala, I. Bargatin, and A. P. Raman, Multi-scale photonic emissivity engineering for relativistic lightsail thermal regulation, arXiv preprint arXiv:2106.03558 (2021).

[34] E. Ressouche, V. Simonet, B. Canals, M. Gospodinov, and V. Skumryev, Magnetic frustration in an iron-based cairo pentagonal lattice, Phys. Rev. Lett. **103**, 267204 (2009).

[35] C. Zhang, M. Giroux, T. A. Nour, and R. St-Gelais, Radiative heat transfer in freestanding silicon nitride membranes, Phys. Rev. Applied **14**, 024072 (2020).

[36] P. Van Zwol, D. Vles, W. Voorthuijzen, M. Péter, H. Vermeulen, W. Van Der Zande, J. M. Sturm, R. W. E. van de Kruijs, and F. Bijkerk, Emissivity of freestanding

membranes with thin metal coatings, Journal of Applied Physics **118**, 213107 (2015).

[37] R. Gao, Y. Kim, L. Kim, M. D. Kelzenberg, O. Ilic, and H. A. Atwater, Self-stabilizing silicon nitride lightsails, in *Conference on Lasers and Electro-Optics* (Optical Society of America, 2020) p. SF3J.6.

[38] X. Chen, C. Chardin, K. Makles, C. Caër, S. Chua, R. Braive, I. Robert-Philip, T. Briant, P.-F. Cohadon, A. Heidmann, T. Jacqmin, and S. Deléglise, High-finesse fabry-perot cavities with bidimensional si3n4 photonic-crystal slabs, Light: Science Applications **6**, e16190 (2017).

[39] R. A. Norte, M. Forsch, A. Wallucks, I. Marinković, and S. Gröblacher, Platform for measurements of the casimir force between two superconductors, Phys. Rev. Lett. **121**, 030405 (2018).

[40] J. Bolk, *ArF scanner lithography for InP photonic integrated circuit fabrication*, Ph.D. thesis, Applied Physics (2020).

[41] J. Bergstra, B. Komer, C. Eliasmith, D. Yamins, and D. D. Cox, Hyperopt: a python library for model selection and hyperparameter optimization, Computational Science & Discovery **8**, 014008 (2015).

[42] Z. Lin, V. Liu, R. Pestourie, and S. G. Johnson, Topology optimization of freeform large-area metasurfaces, Opt. Express **27**, 15765 (2019).

4

DISCUSSION & RECOMMENDATIONS

In this work, the conventional MMA-TO method is compared with a novel CNN-TO algorithm for the design of a lightsail considering practical manufacturing and operation constraints. The results show that the MMA-TO is marginally better for smaller design problems, but CNN-TO performs better overall, especially for high-dimensional problems (fine grid discretizations). Despite MMA-TO being well-documented and simple to implement, and although its performance can improve when performing a hyperparameter search, the novel CNN-TO outperforms MMA-TO for different problems without changing the neural network architecture or its hyperparameters. However, the complexity and number of hyperparameters might reveal a limitation for future applications of the CNN-TO method in different contexts. This has not been investigated in this work.

We conjecture that the CNN-TO method owes its success to the choice of neural network architecture, which in this work was based on the CNN presented in Lempitsky et al., 2018. This architecture was first proposed in the context of topology optimization by Hoyer et al., 2019. In this thesis this methodology was adapted to the optimization of PhC's for the lightsail problem. A similar hyperparameter search as proposed for the MMA-TO can be implemented by HyperOpt (Bergstra et al., 2015) to make the CNN more specific to the problem. However, not having to modify the original CNN to get good results indicates the generality of the framework.

By changing the application from structural engineering to lightsail design, additional continuous optimization parameters needed to be added to the CNN-TO. This work chooses to implement the variable in the CNN with a separate branch that only uses one neuron. However, there are multiple ways these variables could be implemented. For example, it could be favourable to interlink the extra variable with additional layers of the CNN or remove it from the CNN and optimize them with a separate optimizer.

Furthermore, this work also assessed the influence of the initialization on the results obtained by both methods. For MMA-TO, the initial solution can be easily imple-

mented as a direct input in the optimizer. For CNN-TO, the initial design and the initialization of the CNN parameters are inter-dependent. Initialising the CNN to output a sheet or vacuum initial design can be done in multiple ways and can have a major effect on the method's performance. Additionally, initializing the CNN to output a specific shape would be unpractical as the relationship between all the CNN variables and the output is non-transparent. A convergence study has shown that the dependency on the initial solution is higher for the CNN-TO compared to the MMA-TO. Nevertheless, for both methods, multiple optimizations for different seeds need to be performed to get to a good solution. Perhaps additional investigations on the impact of initialization on the optimization process might be relevant for future work.

The final designs produced by the CNN-TO method show that the objective and constraints have a significant impact on the design. Multiple objectives or constraints obtained from practical considerations need to be implemented to obtain producible designs that can be tested, allowing for model verification. Only then unforeseen problems might arise. For future work, implementing production constraints (e.g. minimum feature size and minimum radius) within the TO might be relevant. Having designs with $\approx 1\mu$m feature sizes will push the cost down and increase the production speed as standard optical lithography can be used. The optimization performed for SiN indicates that optimizing for different materials can significantly change the final design. The different material properties will result in a different trade-off for the Figure of Merit. Additionally, it can also change the convexity of the optimization problem. The designs generated for SiN also showed an increased dependency on the constraints, where the area constrained resulted in a design with a lower loss compared to the unconstrained optimization. For future work, the effects of material properties on the optimization problem can be investigated to make the optimizer problem-specific.

ACKNOWLEDGEMENTS

Firstly, I want to thank Dr. M.A. Bessa and Dr. R.A. Norte for their guidance throughout the whole project. Dr. M.A. Bessa and Dr. R.A. Norte introduced me to the fields of computational research and photonics, respectively. They helped me approach the work critically and systematically, contributing to my development as a researcher. The many discussions we had encouraged me to critically think about the project from different perspectives and were crucial to getting the work to a higher level. Furthermore, I want to thank the Bessa and Norte research group members for the exciting discussions and introduction to new techniques.

Next, I want to thank Dr.Ir. M. Langelaar as the final member of the thesis committee, for the time and effort put in assessing the thesis.

At last, I want to thank my friends and family that supported me throughout the project.

A

SETTING UP THE PHC TO

A.1. RELAXATION FACTOR

This appendix elaborates on the working principle of the relaxation factor introduced in Jin et al., 2020, to help the convergence of the optimization. The TO algorithm proposed in Jin et al., 2020 is a TO algorithm based on the method of moving asymptotes (MMA) principle. The MMA optimizer is not well behaved when optimizing structures made from a high refractive index material. These materials result in many narrowband resonance peaks when used to optimize a PhC. A relaxation factor (Q), which adds an imaginary absorption loss to the material, is introduced to cope with this. The imaginary absorption broadens the high resonance response. This facilitates the convergence of the simulation when using a small Q (e.g. $Q \approx 50$), but if $Q \to \infty$ it becomes an actual scattering problem. Figure A.1 illustrates this effect on the calculated reflectivity spectrum for a PhC that is not fully optimized, as this is representative of what the optimizer encounters in the first iterations.

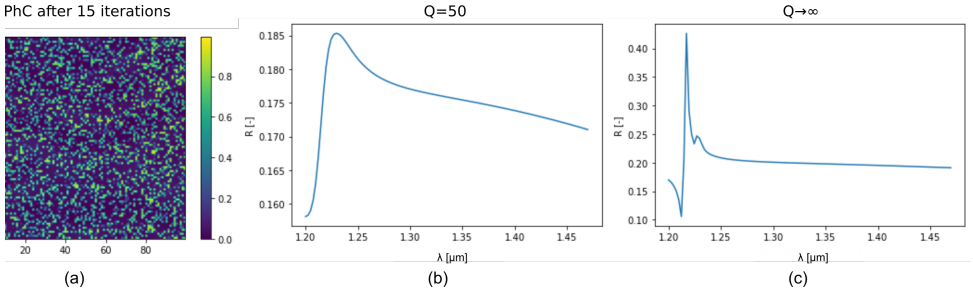

Figure A.1: Reflectivity of a PhC calculated over the operating bandwidth with relaxation factors (Q) of 50 (b) and infinity(c) for a non-optimized PhC (a). λ is the wavelength of the incident light.

It should be noted that when calculating the spectrum with $Q \to \infty$ that it obtains sharp features and the reflectivity values are higher than when calculated with a lower

A

Q. Thus, the reflectivity spectrum obtained with a Q value of 50 is a smoothened version of the one calculated with large Q, resulting in a converged optimization. This relaxation factor is used when discovering solutions via TO by first optimizing with a low Q to ensure convergence, followed by a second optimization where $Q \to \infty$ in the hope of reaching closer to a true optimum.

A.2. STOPPING CRITERION

A commonly used stopping criterion is the relative tolerance (RelTol), as presented in Equation (A.1). The relative tolerance for the function evaluation (acceleration distance D) is taken as the stopping criteria, following Hoyer et al., 2019 and implemented in the method of Jin et al., 2020.

$$RelTol = \frac{(f_n(x) - f_{n+1}(x))}{max(|f_n(x)|, |f_{n+1}(x)|, 1)} \tag{A.1}$$

For most optimizations the relative tolerance is set to 10^{-6} and the maximum amount of iterations is set to 1000 and 100 for $Q = 50$ and $Q \to \infty$ respectively. This can vary for more complex optimizations, but in that case the values are explicitly mentioned in the appropriate location.

A.3. CONVERGENCE STUDY

A convergence study was performed to choose the required grid size for the physics solver (RCWA). However, TO is often mesh dependent, which means that a different mesh can result in a different solution. A study was performed for one seed and one problem (i.e. $t = 107$ nm). The stopping criterion for the optimization is mentioned in Section A.2. The pixel grid was $N \times N$ where N varies from 40 to 400. The optimization has a variable mesh size as the period λ is an optimization variable and can be determined by dividing the period by the grid size N. The resulting designs and the number of iterations are presented in Figure A.3 and Table A.1 respectively.

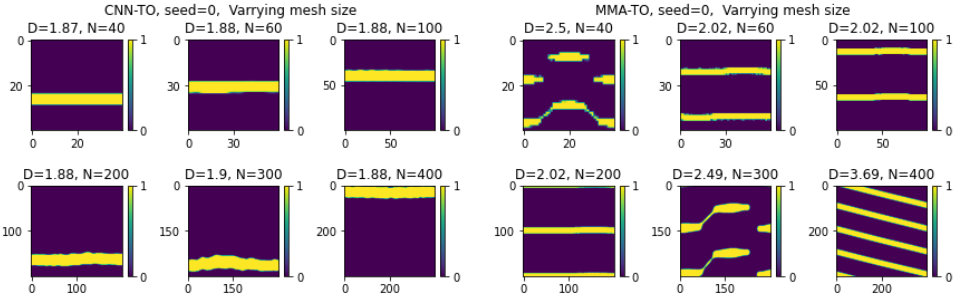

(a) Designs from the CNN-based TO

(b) Designs from the MMA-based TO

Figure A.2: The resulting designs from CNN-based TO and MMA-based TO, for t is 107 nm and N is 100 till 400.

Figure A.2a shows that the resulting designs from the CNN-TO converge to the same design. However, the MMA-TO converges to other optima for different grid sizes. So it

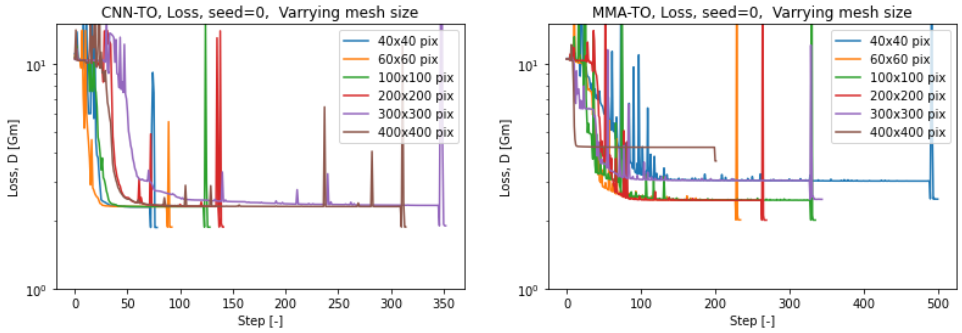

(a) CNN-based TO

(b) MMA-based TO

Figure A.3: The resulting designs from CNN-based TO and MMA-based TO, for t is 107 nm and N is 100 till 400.

seems that the CNN-TO is less mesh dependent than the MMA-TO for these optimization parameters. Notably, the position of the design does not matter because it is a structure with periodic boundary conditions. The loss history for both methods is presented in Figure A.3. It should be noted that all optimizations were terminated by reaching the minimum relative tolerance. The number of iterations and the obtained acceleration distance D are presented in Table A.1. The CNN-TO shows a clear trend in which the larger problems require more iterations than the smaller problems. However, this is not the case for the MMA-TO as not all the designs generated are clear straight line. This can be solved by decreasing the relative tolerance for the optimizations considering a large design space, as the difference between iterations becomes less and more iterations are required to fully converge.

Table A.1: The acceleration distance (D) and number of iterations (it.) with varying mesh sizes for t is 107 nm and one randomization seed.

N [pix.]	**MMA TO**		**CNN TO**	
	D [Gm]	It. [-]	D [Gm]	It. [-]
40	2.49	501	1.87	79
60	2.02	235	1.88	93
100	2.02	336	1.88	129
200	2.02	270	1.88	142
300	2.49	345	1.90	353
400	3.69	202	1.88	315

A.4. BASELINE OPTIMIZATION

The optimization from Jin et al., 2020 is recreated to be used as a baseline. Unfortunately, not all optimization parameters were provided, making recreating the work non-trivial. The original optimization and replicated work is presented in Fig. A.4. These results are

obtained by taking the best optimization from 10 different seeds.

The optima differ between 1% and 9% when compared to data provided in the published article. These variations can result from a reading error from the original data and different optimization parameters not disclosed in the publication. However, the variation is considered acceptable. In this work, the recreated data are used as the baseline and the method is referred to as MMA-TO. Notably, the solution for the thickness of 30 nm diverges significantly. In the original TO, the optimization is initialized as voided material (vaccuum), a uniform slab of material or a random distribution. In this work, it is chosen that for simplicity the designs are only optimized from random distribution. The original optimum can be reached when using an alternative initial solution.

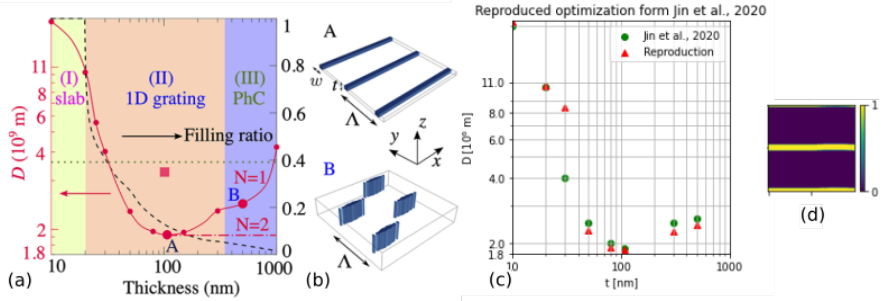

Figure A.4: (a) The original optimization performed in Jin et al., 2020 for the unit-cell of a lightsail made of crystalline silicon, following the Starshot parameters. (b) The related designs to the best optima found in the original optimization. (c) The best results form the replicated optimization obtained from 10 different seeds. (d) representative best design for t ≥ 50 nm.

B

IMPLEMENTING THE CNN-TO

B.1. IMPLEMENTING DESIGN VARIABLES IN THE CNN-TO

The CNN architecture proposed in Hoyer et al., 2019 is modified to accommodate the periodicity (Λ) of the PhC in the optimization, which is a continuous variable that should not benefit from processing through convolutional layers. Figure B.1 presents two different neural network architectures that were considered.

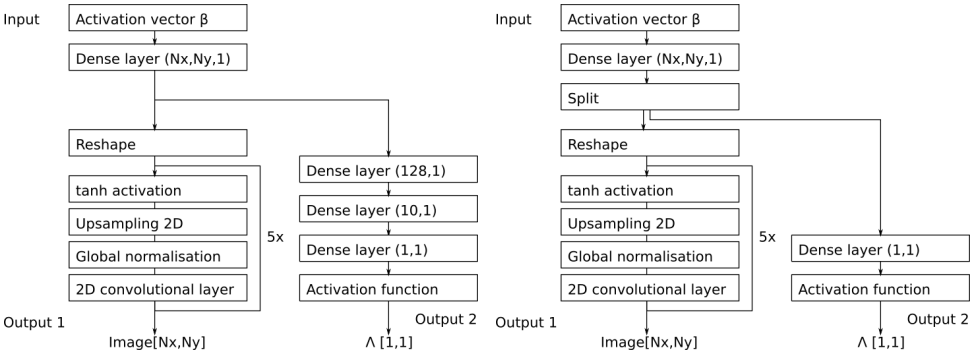

(a) CNN architecture A. The first dens layer is fully connected to a separate branch holding dens layers to implement the periodicity.

(b) CNN architecture B. One element is added to the first dense layer, which is split into a separate branch holding one dense layer consisting of one node.

Figure B.1: Two different implementations for the periodicity within the CNN.

In Figure B.1b the tensor obtained from the first dense layer is split in two, where one of the parts is just a scalar – a (1,1) tensor – that is used as an input to the new dense layer that predicts periodicity (Λ). The other part is a tensor that continues to the original architecture. This solution is called Architecture B (Figure B.1b). A different approach is shown in figure B.1a, where the output tensor from the first dense layer is used as input to three other dense layers to obtain Λ (Architecture A). The benefit of architecture B is its simplicity as it does not introduce many new variables. However,

Table B.1: The acceleration distance form the best optimization ($\overset{*}{D}$), its variance (s^2) and the average amount of iterations ($\bar{i}$) for 3 different seeds for CNN architecture A and B. The absolute function is the activation function.

	Architecture A			**Architecture B**		
t [nm]	$\overset{*}{D}$ [Gm]	s^2	$\bar{i}$[-]	$\overset{*}{D}$ [Gm]	s^2	$\bar{i}$ [-]
10	20.9	0.0	24	20.9	0.0	23
20	10.5	0.0	24	10.5	0.0	23
30	8.41	0.0	22	8.40	0.0	23
50	8.03	0.0	26	2.27	0.0	247
80	2.04	0.03	406	1.92	0.0	220
107	2.35	0.04	424	1.87	0.0	180
300	32.1	0.3	501	0.0	1.2	407
500	2.91	162	336	2.81	0.0	314

using architecture A could result in better predictions because it is densely connected to the first dense layer, which increases expressivity of the network. It should be noted that a thorough architectural search has not been performed as this was not the main focus of the work. Table B.1 shows the results from the optimization of a PhC to compare the different architectures. It should be noted that doing this experiment for three seeds can only give an indication of the performance for the methods. The table shows that for the thicknesses 10 nm to 30 nm, both methods result in the same optimum. However, for the other problems architecture B results in a better design and has less variance for the best design. Furthermore, the amount of iterations used by the optimizer to find the optimum using architecture B is less for most of the problems. Therefore, architecture B is chosen to be used for the rest of the work.

From the experiment a more general formulation can be constructed for adding scalar design variables to the CNN. A schematic overview is presented in figure B.2. This figure shows that to accommodate a new variable a new branch can be generated within the CNN.

B.2. CHOICE OF ACTIVATION FUNCTION

The choice of the activation function within the CNN can have a significant impact on the output. Unfortunately, finding an appropriate activation function is non-trivial as the interaction between the activation function and the CNN is hard to predict. The activation function can be used to transform the values from the input of the neurons of the CNN, which can be any positive or negative number, on to a final output value.

In this work, the proposed CNN from Hoyer et al., 2019 is modified to include the period (Λ) of the PhC as an optimization parameter. In Jin et al., 2020 this design variable is constrained ($0 > \Lambda \leq 3.6\mu m$). These constraints can be reproduced by using appropriate activation functions within the CNN. Since Λ needs to be positive, this can be achieved using activation functions such as the RELU, ELU and absolute (Abs) function because they ensure that is greater than zero, as shown in Figure B.3. The tanh function can be implemented to additionally include a maximum constraint. Therefore, different

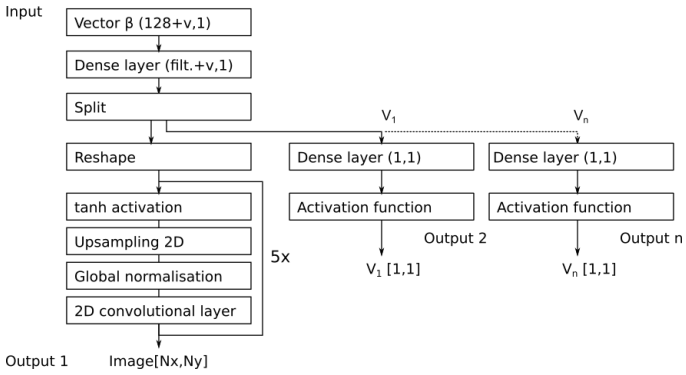

Figure B.2: Generic example for adding extra design variables to the CNN. Filt. is a predefined number of filters in the CNN, v is the amount of extra variables and β is the activation function used as an input.

activation functions for the periodicity output were considered by performing optimizations for three different seeds and comparing the outcomes. It should be noted that using three seeds for this comparison will only give an indication of the performance difference. Note that the ELU and tanh functions were translated vertically to ensure the output is greater than zero (see Figure B.3).

The best acceleration distance D and lowest variance from these optimizations are presented in Table B.2. It can be seen that the tanh function resulted in the worst obtained optima, and the ReLU and ELU and Abs functions obtained similar best designs. From these four activation functions, the Abs resulted in the best designs with the least variance. However, this function can not impose a maximum to the design variable.

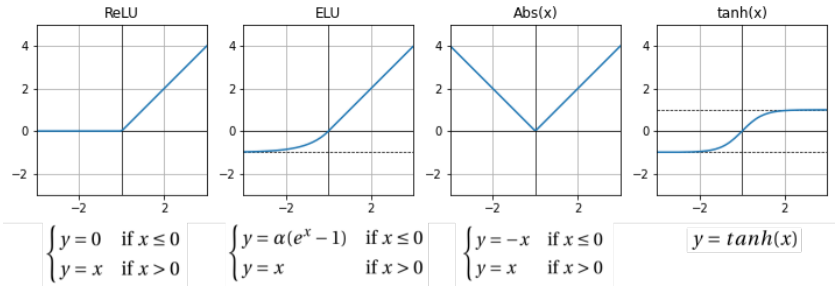

Figure B.3: Four different activation functions used to implement periodicity in the TO.

Because the Abs did not comply with all requirements, the tanh is modified (tanh*) to be more suitable for the optimization problem. Due to the modifications, the tanh* not only allows for the output to be greater than zero and the constraining of the output, but it also allows to influence the initial solution by transposing it in the x-direction. The tanh* is presented in Equation (B.1). In this equation, δ is the difference between the maximum and minimum values. α is defined in such a way that the middle part of the function is 45° with the y-axis. x_0 is the initial solution. Figure B.4 shows an example

Table B.2: The best ($\overset{*}{D}$) optimization and the variance (s^2) from 3 different seeds for different activation functions. tanh* is a modified hyperbolic tangent.

	tanh		**ReLU**		**ELU**		**Abs**		**tanh∗**	
t [nm]	$\overset{*}{D}$ [Gm]	s^2	$\overset{*}{D}$ [Gm]	s^2	$\overset{*}{D}$ [Gm]	s^2	$\overset{*}{D}$ [Gm]	s^2	$\overset{*}{D}$ [Gm]	s^2
10	20.9	0.0	20.9	0.0	20.9	0.0	20.9	0.0	20.9	0.0
20	10.5	0.0	10.5	0.0	10.5	0.0	10.5	0.0	10.5	0.0
30	8.41	0.0	8.41	0.0	8.41	0.0	8.40	0.0	8.4	0.0
50	2.52	0.02	2.27	7.3	2.30	2.0	2.27	0.0	2.27	0.06
80	2.28	0.01	1.92	9.5	1.92	0.3	1.92	0.0	1.92	0.3
107	2.28	0.01	1.87	12	1.87	12	1.87	0.0	2.01	0.2
300	2.85	0.06	2.50	211	2.50	26	2.28	17	2.28	0.01
500	2.75	0.01	2.81	204	2.81	0.0	2.82	0.0	2.44	0.03

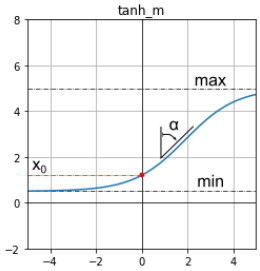

Figure B.4: Example of modified tanh (tanh*) with maximum and minimum set to 0.5 and 5 respectively and the initial solution (x_0) to 1.2.

of the implementation of tanh*. In this example, minimum and maximum are set to 0.5 and 5 respectively, and the initial solution to 1.2.

$$\delta = Max - Min \tag{B.1a}$$

$$\alpha = \tanh^{-1}\left(\frac{2(x_0 - Min)}{\delta} - 1\right) \tag{B.1b}$$

$$y = \frac{1}{2}\delta\left(\tanh\left(\frac{2x}{\delta} + \alpha\right) + 1\right) + Min \tag{B.1c}$$

The results obtained by the transformed tanh* are also included in Table B.2. The table shows that using Abs or tanh* results in comparable results. However, tanh* is chosen as the activation function as it allows the most control over the design variable by imposing the necessary constraints.

B.3. EFFECT ON OUTPUT

This section will give an example of the variability of the CNN-TO with the optimization parameters. The optimizations presented in Figure B.5a and Figure B.5b have the sinh

intermediate density penalization value of 1 and 3 respectively, to promote a binary design (Deaton and Grandhi, 2014). The intermediate values between zero and one are penalized more with a high penalty value. In the optimization, the other optimization parameters and the MMA-TO are identical. The figures show more than 20% difference in the number of optimization iterations between each CNN-TO. The large penalty makes it difficult for the TO to flip pixels properly as the penalty is impeding smooth transition.

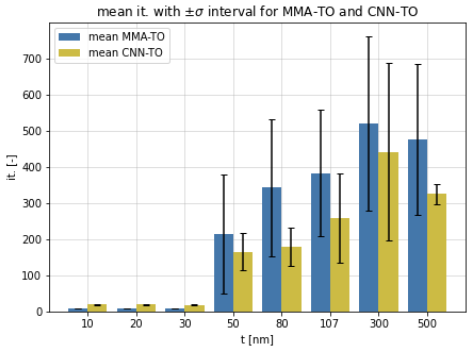

(a) Mean number of iterations with penalty of 1.

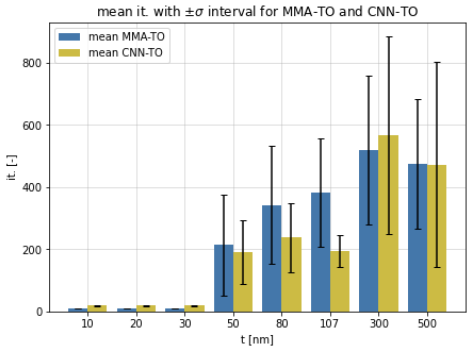

(b) Mean number of iterations with penalty of 3.

Figure B.5: Two different implementations for the periodicity output of the CNN

C

DESIGNS AND LOSS FUNCTIONS FROM OPTIMIZATION RUNS

C.1. OPTIMIZATION OF PHC WITH FIXED THICKNESS

REPRESENTATIVE DESIGNS

The results from the experiments to compare the performance of the CNN-TO and the MMA-TO are presented below. Figures C.1 to C.4 present the loss functions and the resulting designs for 4 different seeds for the CNN-TO and MMA-TO. In the experiment 10 seeds were used. The presented graphs are representative for the other solutions generated from the other seeds. The results generated by the CNN-TO are shown in Figures C.1 to C.2 and the results from the MMA-TO are presented in Figures C.3 to C.4.

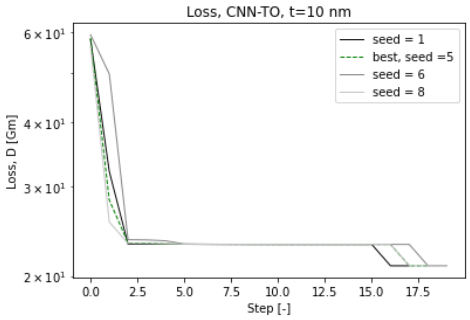

(a) t=10 nm

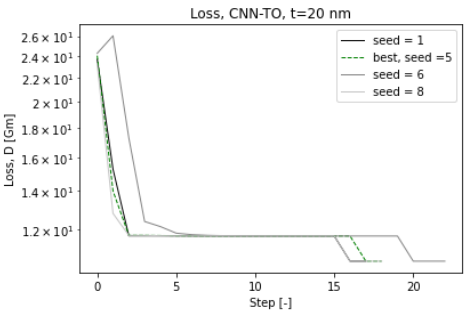

(b) t=20 nm

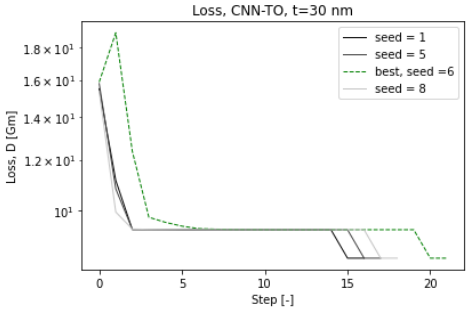

(c) t=30 nm

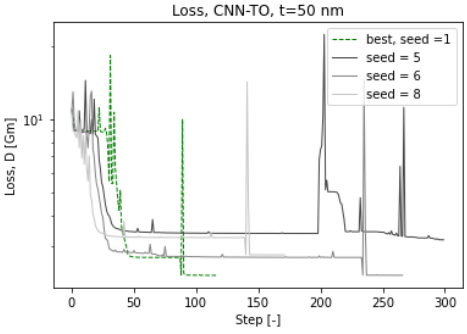

(d) t=50 nm

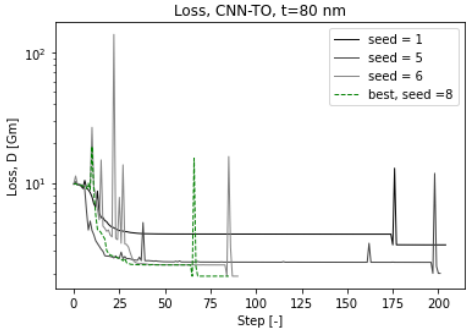

(e) t=80 nm

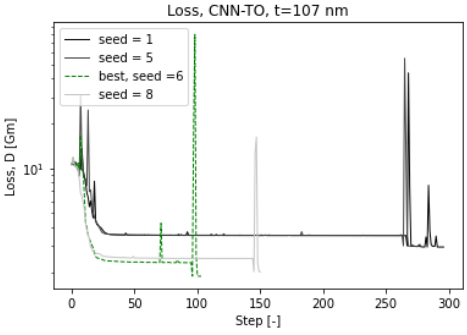

(f) t=107 nm

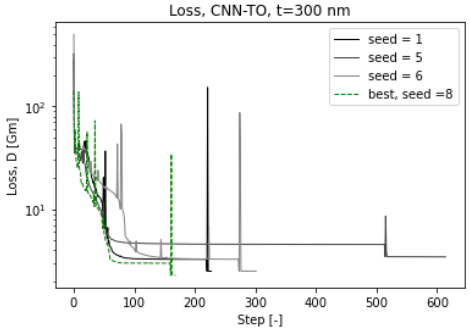

(g) t=300 nm

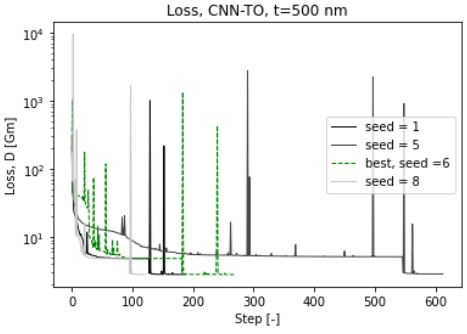

(h) t=500 nm

Figure C.1: Loss functions of optimization with fixed thickness and varying seeds. Optimization was executed with the CNN-TO and architecture B.

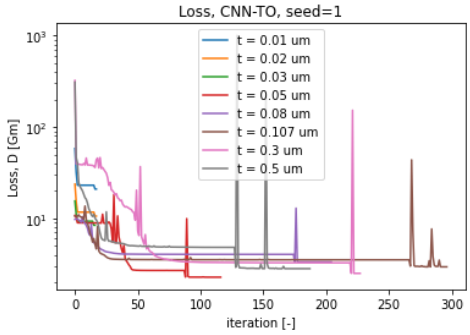

(a) Loss from seed 1

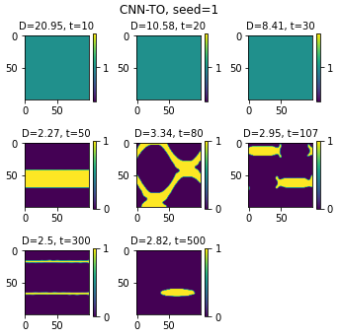

(b) Designs from seed 1

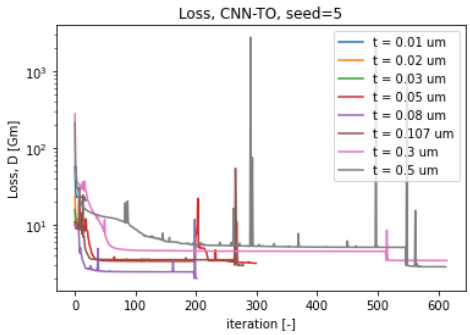

(c) Loss from seed 5

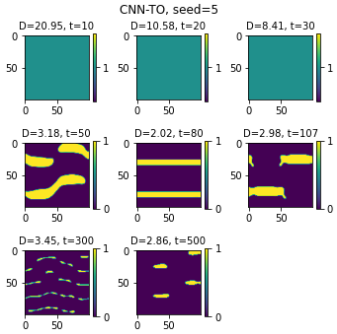

(d) Designs from seed 5

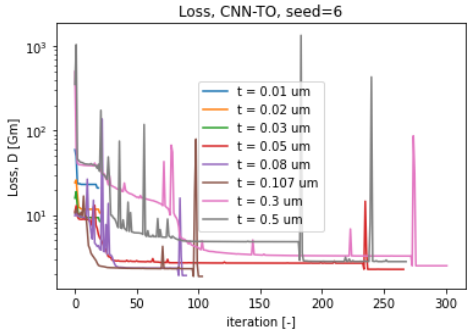

(e) Loss from seed 6

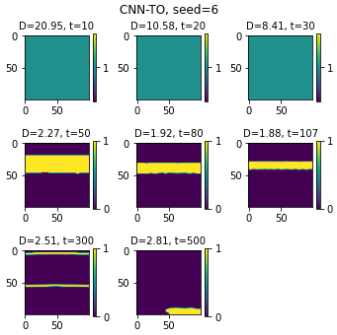

(f) Designs from seed 6

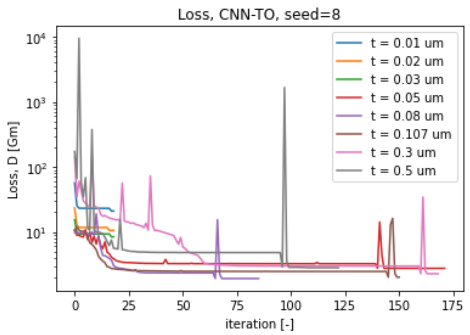

(g) Loss from seed 8

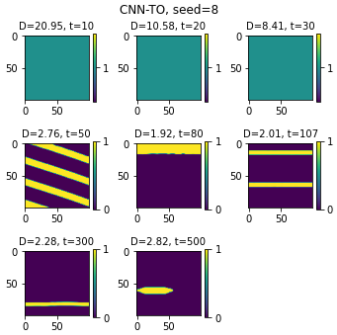

(h) Designs from seed 8

Figure C.2: Loss functions and designs of optimizations with fixed seed and varying thickness. Optimization was executed with the CNN-TO.

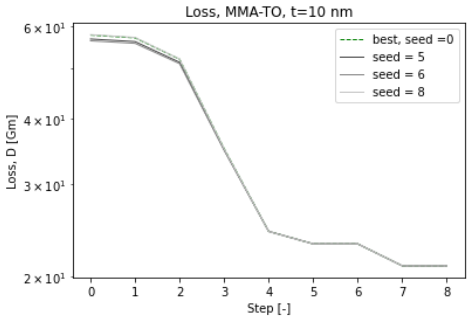

(a) t=10 nm

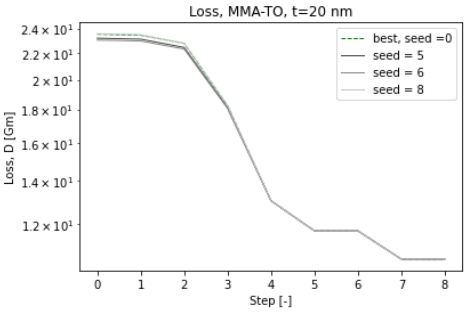

(b) t=20 nm

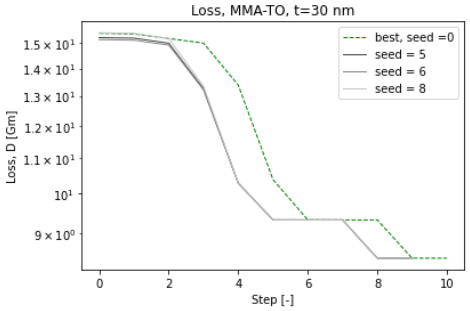

(c) t=30 nm

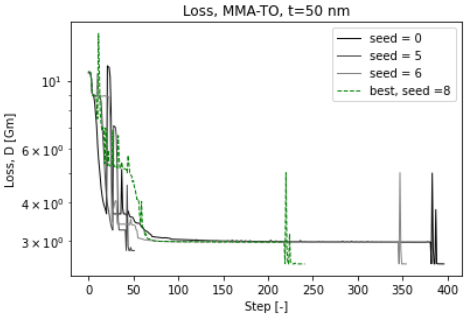

(d) t=50 nm

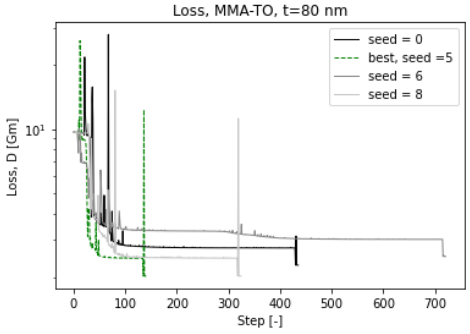

(e) t=80 nm

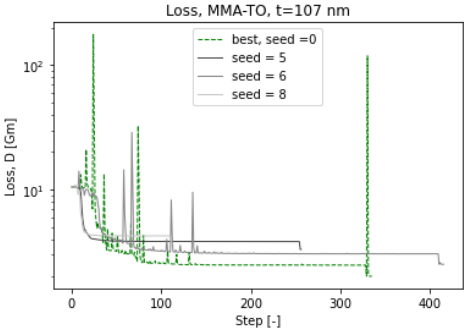

(f) t=107 nm

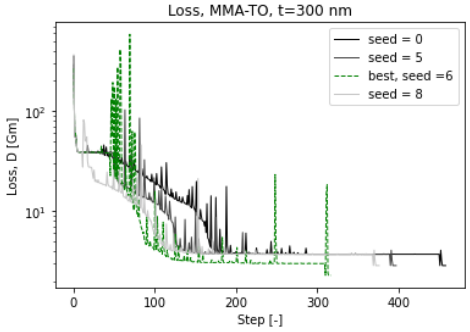

(g) t=300 nm

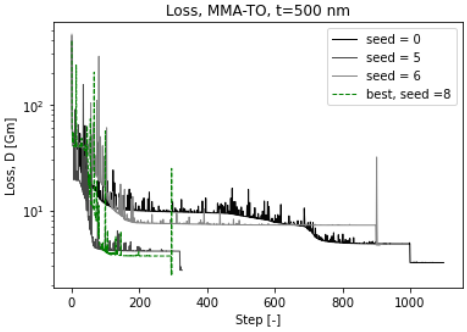

(h) t=500 nm

Figure C.3: Loss functions of optimization with fixed thickness and varying seeds. Optimization was executed with the MMA-TO.

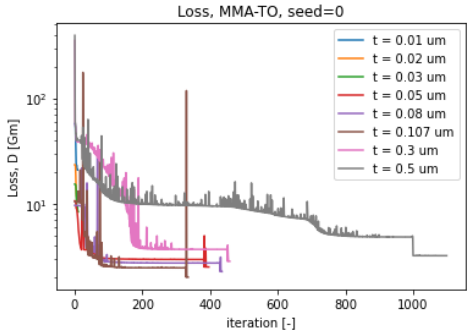

(a) Loss for seed 0

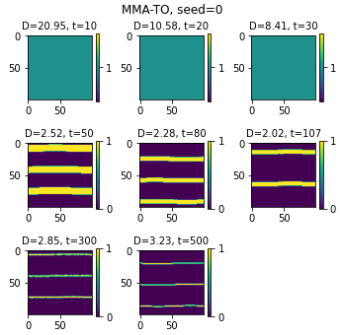

(b) Designs for seed 0

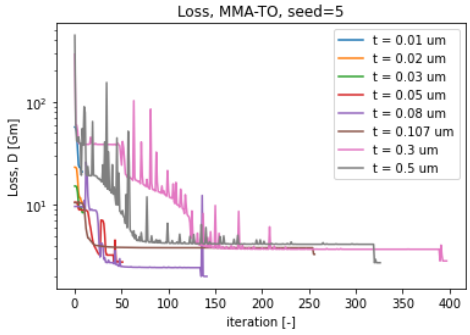

(c) Loss for seed 5

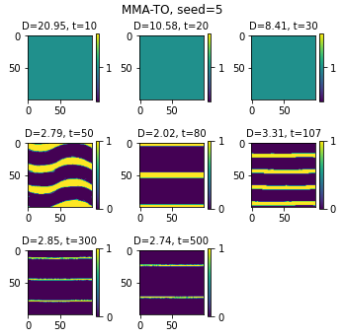

(d) Designs for seed 5

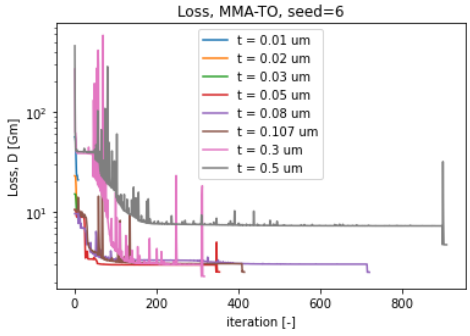

(e) Loss for seed 6

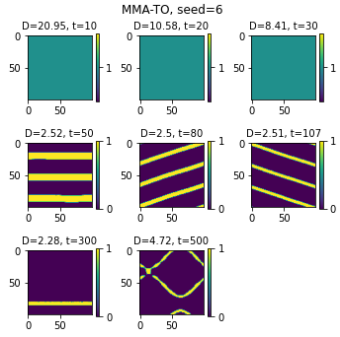

(f) Designs for seed 6

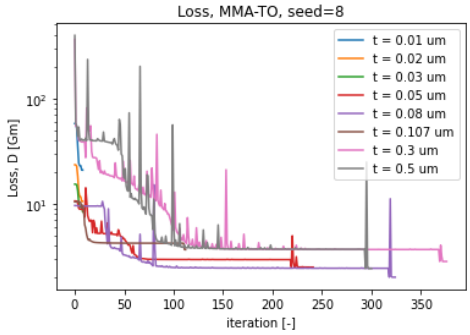

(g) Loss for seed 8

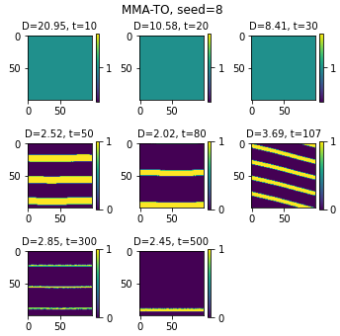

(h) Designs for seed 8

Figure C.4: Loss functions and designs of optimizations with fixed seed and varying thickness. Optimization was executed with the MMA-TO.

D

PRACTICAL CONSIDERATION FOR THE LIGHTSAIL OBJECTIVE

D.1. ALIGNMENT WITH THE LASER

Fig. D.1 shows the resulting best design when optimizing a PhC for only one polarisation direction of the incident laser. The FOM need to be reconsidered as the design will lose its performance when rotated around its normal (ϕ). Furthermore, the string design is not practical to fabricate. These issues have been addressed by incorporating two different alignment directions (ϕ and θ) in the FOM. First, the alignment with the laser beam's polarization (ϕ) is considered because the string design result from the laser being a linear polarised plane wave. The polarisation is incorporated by taking the mean acceleration distance D for two perpendicular polarization directions (e.g. ϕ is 0° and 90°). Additional, the thickness (t) of the PhC is added as an optimization variable to generalize the TO further. The new optimization formulation is presented in Equation (D.1). The number of integration points used for calculating the reflectivity over the operating bandwidth was changed from 24 to 12 to keep the computational time for the objective the same while adding an extra polarisation direction. The optimization was performed with both number of integration points. Although the final obtained acceleration distance is slightly lower (around 0.4 Gm) when using 12 integration points, the optimizer resulted in the same optimal designs. This was chosen to be acceptable and in the following optimizations, 12 integration points are used for the reflectivity calculations, except when explicitly specified differently.

$$
\begin{aligned}
\min_{x_{ij},\Lambda} \quad & D(R(x_{ij},\Lambda)) \\
\text{subject to} \quad & \nabla \times \mathbf{E} = -i\omega\mu_0\mathbf{H}, \quad \nabla \times \mathbf{H} = i\omega\epsilon_0\epsilon\mathbf{E} \ , \\
& 0 \le x_{ij} \le 1 \ \forall (i,j), \\
& 0.1\mu m \le \Lambda \le 3.6\mu m. \\
& 0.01\mu m \le t \le 1\mu m.
\end{aligned}
\tag{D.1}
$$

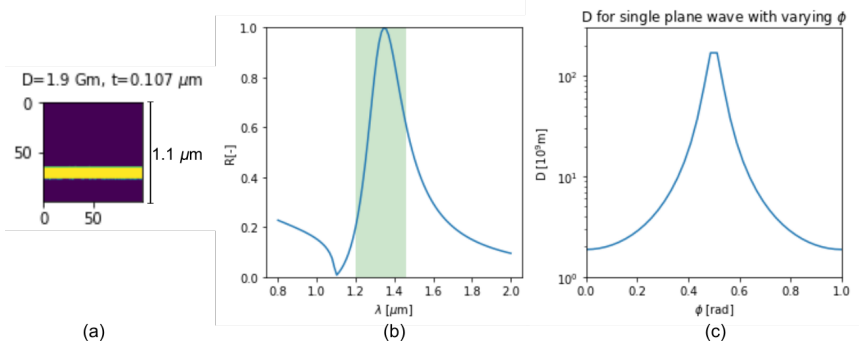

Figure D.1: Best design resulting form TO of PhC for one polarisation direction. (a) Best design, where yellow is the material and blue vacuum. (b) Reflectively of the PhC for different wavelengths, green area indicates the operating bandwidth. (c) Acceleration distance of the PhC for different polarisation directions (ϕ).

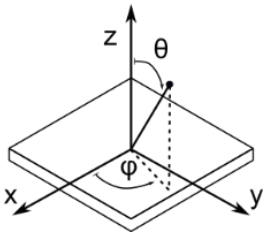

Figure D.2: Axis definition for the PhC.

This resulted in a two-dimensional PhC with square holes. In practice, the normal of the plane could also be rotated by θ with respect to the incoming laser. This was included in the FOM by taking the mean of D for six different illumination directions. For each orientation of ϕ three angles for θ were applied (θ is 0°, 5°and 10°). Additionally, a weighted average was applied for θ being 0°, 10°, and 20° with weights of 5, 3 and 1, respectively. However, incorporating the angle θ did not result in new best designs. This could result from the way the reflectively is considered in the simulation. For the FOM the total reflected light from the PhC is calculated and the direction of the reflected light is not considered. In the literature the direction of the reflected light is considered in the FOM to generate a restoring force when the sail is perturbed from the ideal position (Ilic and Atwater, 2019; Salary and Mosallaei, 2020).

D.2. COOLING INCORPORATED IN OPTIMIZATION

The area of the sail is the geometric parameter influencing the maximum temperature T_{max} of the lightsail, as it is inversely related. The cooling is included in TO by applying an area constraint. For separate optimizations the area constraint (A_0) was varied from 40%-60%, the other optimization parameters were not changed. The best design from this optimization is presented in Figure D.4a, which has an A_0 of 45% – this is the maximum value that still converged to a practical design. This design follows a cairo

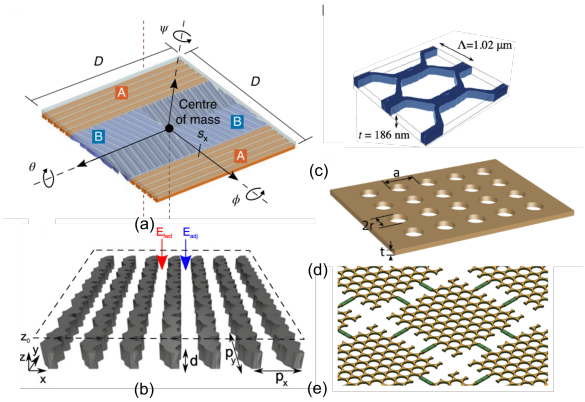

Figure D.3: Different designs proposed in the literature. (a) Ilic and Atwater, 2019, (b) Kudyshev et al., 2021, (c) Jin et al., 2020, (d) Myilswamy et al., 2020, (e) Brewer et al., 2022

pentatonic lattice structure and in literature no equivalent design has been reported. Figure D.3 provides an overview of the commonly proposed designs, consisting out of holes that follow a pentagonal or square lattice or a meta grid consisting out of strings with varying thickness. The maximum temperature of the sail can be calculated with Equation (D.2) (Brewer et al., 2022). In this equation P_{laser} is the power of the laser, α_{sail} the assumed normalized sail absorption, and A_{sail} the area of the sail, $c_1 = 2\pi hc^2$, $c_2 = hc/k_b$, k_b is the Boltzmann constant, h is Planck's constant, c is the speed of light, ϵ_{sail} is the emissivity of the sail.

$$P_{laser}\alpha_{sail} = 2A_{sail}\int_{\lambda_0}^{\lambda_1} \frac{c_1}{\lambda^5} \frac{\epsilon_{sail}(\lambda)}{e^{\frac{c_2}{\lambda T_{max}}} - 1} d\lambda \tag{D.2}$$

Figure D.4 shows the maximum temperature T_{max} for different power outputs of the laser. For the calculations ϵ and α are assumed to be constant. Multiple curves for different ϵ values are presented because the variation of this property for different parameters is not well documented in the literature. ϵ is a function of the material thickness, temperature and will vary for different wavelengths (Van Zwol et al., 2015; Zhang et al., 2020). Another uncertainty is the value for α as there is a lack of precision measurements for representative operating conditions Brewer et al., 2022. So, the real value for T_{max} of the c-Si can not be determined. However, depending on the values of ϵ and α the graph shows that it could be the difference of staying under the maximum operating temperature. There are two additional concerns regarding equation D.2. In this equation α and P_{laser} are assumed to be constant which is incorrect because α varies with the wavelength of the light (Chen et al., 2017) and the absorbed power will vary with the reflectivity of the sail. A large part of the laser light will be transmitted though the PhC and not be absorbed because the PhC does not have a 100% reflectivity for it operation bandwidth. In Figure. D.4c the melting temperature of c-Si is shown as the maximum sail temperature. In practice, this is not correct as the material will lose its mechanical properties at lower temperatures.

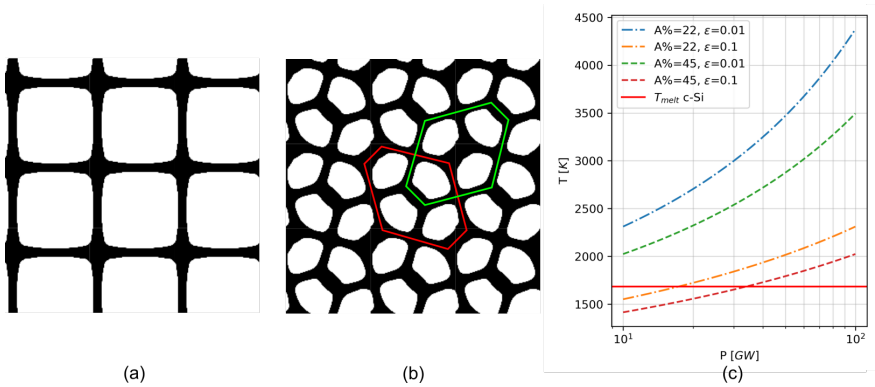

Figure D.4: PhC design, optimized for two orthogonal polarisation directions without (a) and with area constraint of 45% (b) for a c-Si PhC. The designs with area constraint follow a cairo pentatonic lattice indicated with the red and green lines. (c) The maximum temperature for a c-Si PhC for different values for ϵ.

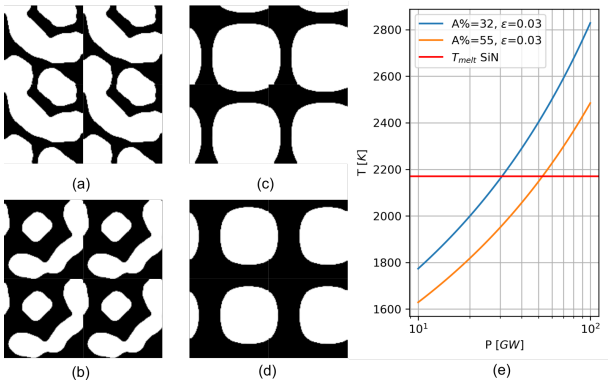

Figure D.5: Designs for optimization for two orthogonal polarization directions for SiN. (a) the best resulting design, (b) the best resulting design with A_0 of 55%. (c) local optima with square hole design, (d) local optima with square hole design and A_0 is 55%. (e) Maximum temperature of best designs (a,b) for varying laser power.

D.3. OPTIMIZATION FOR SIN PHC

In order to consider an alternative material to fabricate the lightsail, additional optimizations for two polarisation directions were also performed for SiN, instead of c-Si. Notably, these optimizations were more prone to be influenced by the initial solution than the ones for c-Si. If the initial solution used for c-Si is considered, the optimizations for SiN led to square hole designs as shown in Figure D.5c,d. The square hole designs resulted in a higher average acceleration distance for $\phi = 0°$ and $\phi = 90$ °.

However, when setting the initial solution for Λ to twice the wavelength and t to 50 nm the design resulted in a semi-circle designs presented in Figure D.5a,b. Although there has not been an intensive study for the effect of the initial solution on the final design, these results show that the optimization behaves differently for SiN than for c-Si as the result of the difference in density and dielectric constant (κ) (Table D.1). The lower

Table D.1: Material properties c-Si and SiN

	ρ [kg/m^3]	κ	
SiN	3100	4	Moura et al., 2018
c-Si	2329	11	Jin et al., 2020

κ makes the difference in reflectivity between the SiN designs less than compared to c-Si. The optimization process also has worse convergence because there is less difference in acceleration distance between the different designs.

The designs shown in Figure D.5a,b are not symmetric, which could lead to a varying reflectivity for different polarisation angles. Figure D.6 shows the reflectivity and the acceleration distance D of both designs for a single incident plane wave for varying polarisation angels ϕ. It can be seen that these designs have a highly fluctuating reflectivity within the operating bandwidth. Additionally, the acceleration distance for these designs is significantly less for polarisation direction other than $\phi = 0°$ and $\phi = 90°$. Strikingly, the reflectivity and the acceleration distance of the square hole designs fluctuate less than the semi-circle designs, resulting in an overall lower acceleration distance over the whole range from $\phi = 0°$ to $\phi = 90°$ (Figure D.7). The performance of other designs with different area constraints can be compared over the whole range of ϕ. This resulted in the new best design presented in Figure D.8, which has the lowest mean acceleration distance for all angles of ϕ. Strikingly, this design has even a lower acceleration distance than the square hole design, optimized without any area constraint. This indicates that the optimizer found a local optimum when no area constraint was applied.

Additionally, the highly fluctuating reflectivity spectrum presented in Figure D.6 would require a higher number of integration points to prevent an aliasing effect. The difference between the number of integration points, as presented in Figure D.9, is much more significant for the SiN designs than for c-Si. An additional optimization was performed using the mean acceleration distance of ϕ is 0°, 45°, 90° and 135°. Furthermore, 24 integration points were used for the reflectivity calculation to address the concerns mentioned above. These additional optimization parameters resulted in the design shown in Figure D.10, which is a two-dimension PhC having almost circular holes. A similar study was also performed for c-Si. However, this did not result in a different design, because the difference in acceleration distance for varying ϕ of a single plane wave was already less than 1%. This design had the benefit of having round features and thick tethers resulting in less stress concentrations.

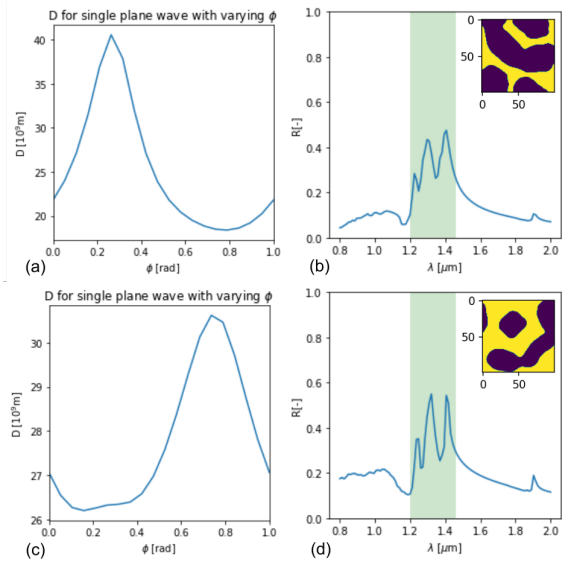

Figure D.6: Best optimized SiN PhC from 5 different randomization seeds for $\phi = 0°$ and $\phi = 90°$ considering thickness t, material density and Λ as optimization parameters. The period Λ is initialised as twice the laser wavelength. (a,c) Reflectivity of the PhC for $\phi = 0°$ and for different wavelengths, where the green area shows the operating bandwidth of the sail, (b,d) the acceleration distance D for the design shown in the upper right corner (yellow is material, blue is vacuum) illuminated by a single polarized plane wave for varying angle (ϕ)

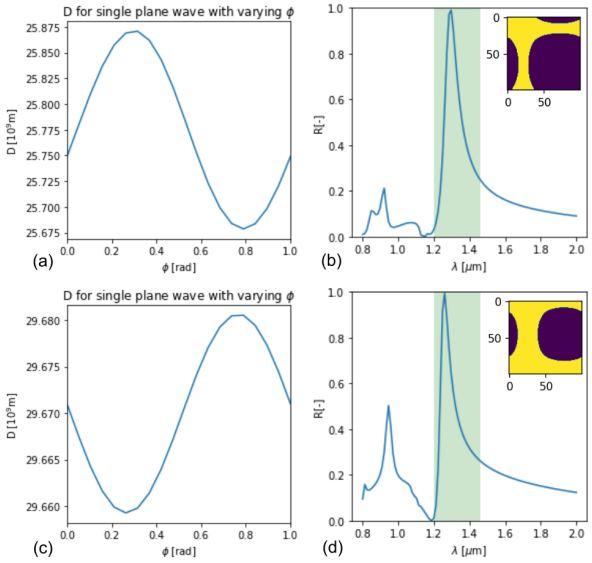

Figure D.7: Best optimized SiN PhC from 5 different randomization seeds for $\phi = 0°$ and $\phi = 90°$ considering thickness t, material density and Λ as optimization parameters. The period Λ is initialised as the laser wavelength. (a,c) Reflectivity of the PhC for $\phi = 0°$ and for different wavelengths, where the green area shows the operating bandwidth of the sail, (b,d) the acceleration distance D for the design shown in the upper right corner (yellow is material, blue is vacuum) illuminated by a single polarized plane wave for varying angle (ϕ)

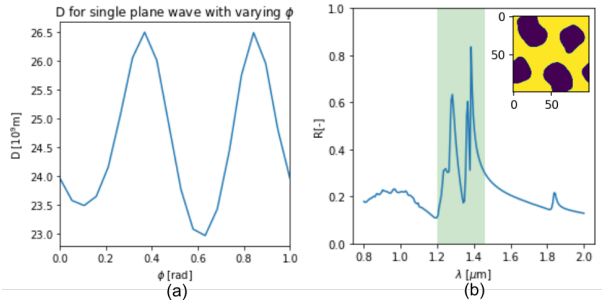

Figure D.8: Best optimized SiN PhC from 5 different randomization seeds for $\phi = 0°$ and $\phi = 90°$ considering thickness t, material density and Λ as optimization parameters and an area constaint of 60%. The period Λ is initialised as twice the laser wavelength. (a) Reflectivity of the PhC for $\phi = 0°$ and for different wavelengths, where the green area shows the operating bandwidth of the sail, (b) the acceleration distance D for the design shown in the upper right corner (yellow is material, blue is vacuum) illuminated by a single polarized plane wave for varying angle (ϕ)

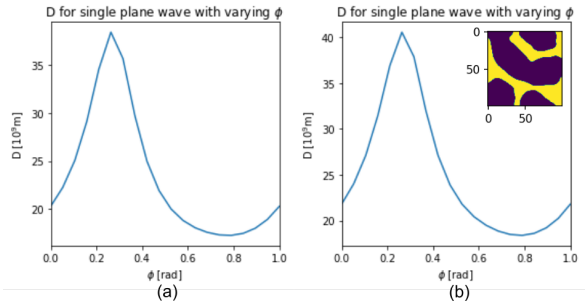

Figure D.9: The acceleration distance D for the design shown in the upper right corner (yellow is material, blue is vacuum) illuminated by a single polarized plane wave for varying angle (ϕ), using 12(a) and 24(b) integration points.

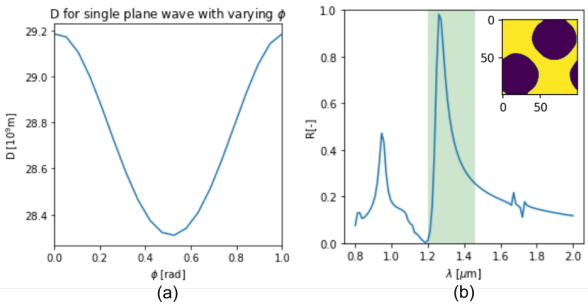

Figure D.10: Best optimized SiN PhC from 5 different randomization seeds for ϕ is 0°, 45°, 90° and 135° considering thickness t, material density and Λ as optimization parameters and a area constraint of 60%. The period Λ is initialised as the laser wavelength. best design using the CNN-TO where yellow is material and blue vacuum, (a) reflectivity of the PhC for $\phi = 0°$ and for different wavelengths, where the green area shows the operating bandwidth of the sail, (b) the acceleration distance D for the design shown in the upper right corner (yellow is material, blue is vacuum) illuminated by a single polarized plane wave for varying angle (ϕ)

BIBLIOGRAPHY

Brewer, J., Campbell, M. F., Kumar, P., Kulkarni, S., Jariwala, D., Bargatin, I., & Raman, A. P. (2022). Multiscale photonic emissivity engineering for relativistic lightsail thermal regulation. *Nano Lett.* https://doi.org/10.1021/acs.nanolett.1c03273

Chen, X., Chardin, C., Makles, K., Caër, C., Chua, S., Braive, R., Robert-Philip, I., Briant, T., Cohadon, P.-F., Heidmann, A., Jacqmin, T., & Deléglise, S. (2017). High-finesse fabry-perot cavities with bidimensional si3n4 photonic-crystal slabs. *Light: Science Applications*, *6*(1), e16190–e16190. https://doi.org/10.1038/lsa.2016.190

Ilic, O., & Atwater, H. A. (2019). Self-stabilizing photonic levitation and propulsion of nanostructured macroscopic objects. *Nature Photonics*, *13*(4), 289–295. https://doi.org/10.1038/s41566-019-0373-y

Jin, W., Li, W., Orenstein, M., & Fan, S. (2020). Inverse design of lightweight broadband reflector for relativistic lightsail propulsion. *ACS Photonics*, *7*(9), 2350–2355. https://doi.org/10.1021/acsphotonics.0c00768

Kudyshev, Z. A., Kildishev, A. V., Shalaev, V. M., & Boltasseva, A. (2021). Optimizing startshot lightsail design: A generative network-based approach. *ACS Photonics*. https://doi.org/10.1021/acsphotonics.1c01352

Moura, J. P., Norte, R. A., Guo, J., Schäfermeier, C., & Gröblacher, S. (2018). Centimeter-scale suspended photonic crystal mirrors. *Opt. Express*, *26*(2), 1895–1909. https://doi.org/10.1364/OE.26.001895

Myilswamy, K. V., Krishnan, A., & Povinelli, M. L. (2020). Photonic crystal lightsail with nonlinear reflectivity for increased stability. *Opt. Express*, *28*(6), 8223–8232. https://doi.org/10.1364/OE.387687

Salary, M. M., & Mosallaei, H. (2020). Photonic metasurfaces as relativistic light sails for doppler-broadened stable beam-riding and radiative cooling. *Laser Photonics Reviews*, *14*(8), 1900311.

Van Zwol, P., Vles, D., Voorthuijzen, W., Péter, M., Vermeulen, H., Van Der Zande, W., Sturm, J. M., van de Kruijs, R. W. E., & Bijkerk, F. (2015). Emissivity of freestanding membranes with thin metal coatings. *Journal of Applied Physics*, *118*(21), 213107.

Zhang, C., Giroux, M., Nour, T. A., & St-Gelais, R. (2020). Radiative heat transfer in freestanding silicon nitride membranes. *Phys. Rev. Applied*, *14*, 024072. https://doi.org/10.1103/PhysRevApplied.14.024072